

# Concave-wall turbulent boundary layers without and with free-stream turbulence

Jiho You, David A. Buchta and Tamer A. Zaki†

Department of Mechanical Engineering, Johns Hopkins University, Baltimore, MD 21218, USA

(Received xx; revised xx; accepted xx)

Direct numerical simulations are performed to contrast turbulent boundary layers over a concave wall without and with free-stream turbulence. Adverse pressure gradient near the onset of curvature leads to sharp decrease in skin friction and intermittent separation. The presence of free-stream turbulence reduces the probability of reverse flow, accelerates the recovery of the boundary layer in the downstream zero-pressure gradient region, and leads to a sustained and appreciable increase in the skin friction. The forcing also promotes the amplification of coherent Görtler structures in the logarithmic layer of the curved-wall boundary layer. Statistically, the spanwise and wall-normal Reynolds stresses intensify and the radial distance between their peaks increases downstream as the Görtler structures expand. The Reynolds shear stress coefficient also increases in the logarithmic layer in contrast to a decrease when a flat-plate boundary layer is exposed to free-stream turbulence. In addition, the more coherent and energetic roll motions in the forced flow promote mixing of free-stream and boundary-layer fluids, where the former is seen more often deep within the buffer layer.

## 1. Introduction

In practical flow configurations, turbulent boundary layers (TBLs) often develop over curved surfaces. The focus in the present study is on concave curvature which induces centrifugal effects in addition to the external pressure gradient. Another important practical consideration is the presence of environmental disturbances, or free-stream forcing, which can appreciably alter the dynamics within the underlying boundary layer. For example, when a flat-plate TBL is buffeted by free-stream turbulence (FST), its thickness and skin-friction coefficient increase appreciably, even when the free-stream fluid has not breached the logarithmic layer (You & Zaki 2019). The present work uses direct numerical simulations (DNS) to probe the combined effects of the concave curvature and FST on the boundary layer. Two simulations are contrasted, and correspond to the turbulent boundary layer on the concave wall developing beneath quiescent and vortical free streams (see figure 1).

### 1.1. Turbulent boundary layer on concave wall

Curved-wall turbulent boundary layers are influenced by three effects (Floryan 1991): i) turbulence changes due to the mean-flow turning, ii) potential formation of coherent Görtler vortices, and iii) the impact of these coherent vortices on the turbulence. The second mechanism is triggered when the boundary-layer thickness (e.g. momentum thickness  $\theta$ ) is comparable to the radius of curvature ( $R$ ). In laminar flows, an instability, due to the gradient of angular momentum in the radial direction, leads to the formation of longitudinal Görtler vortices (Saric 1994; Schrader *et al.* 2011). In turbulent flows,

† Email address for correspondence: t.zaki@jhu.edu

however, Görtler structures are notoriously difficult to identify, which obfuscates precise description. The complexity is compounded when TBLs are exposed to free-stream turbulence: Whether the external forcing will decorrelate the structures or enhance them is uncertain, and how the coupling between the Görtler structures and the finer-scale boundary-layer turbulence will be affected is unknown.

Much of the literature on curved-wall turbulence has focused on conditions with quiescent free streams. Barlow & Johnston (1988a) performed experiments to probe the response of the boundary layer to a sudden onset of concave curvature. They reported that higher momentum eddies move toward the wall, while lower momentum eddies travel away from it. Despite efforts to visualize the streamwise vortices using the colored-dye and laser-induced-fluorescence methods, direct observation of Görtler vortices was difficult; yet enhanced shear stress in the outer BL region suggests their presence. In other works, Hoffmann *et al.* (1985) and Barlow & Johnston (1988b) used a vortex generator to induce large-scale, time-stable roll cells, which produced a coupling between the large-scale outer fluid motions and near-wall turbulence. Barlow & Johnston (1988b) showed that the downwash suppresses the bursting, which induces interactions between sublayer structures and outer-layer eddies, while the upwash enhances the process. However, the connection between naturally occurring Görtler vortices in turbulence (irregularly spaced and temporally intermittent) to those produced by synthetic means is unknown (e.g. Patel & Sotiropoulos 1997).

Lund & Moin (1996) and Arolla & Durbin (2015) numerically modelled the experiment by Barlow & Johnston (1988a). They used large-eddy simulations (LES) to directly probe the longitudinal vortices due to the centrifugal effect. Spatially filtering the turbulence field revealed streamwise-aligned structures inside the TBL above the curved wall, which supports the existence of Görtler structures within the boundary-layer turbulence (Lund & Moin 1996; Arolla & Durbin 2015). However, the degree that the external pressure gradient influences the TBL on the curved surface was not addressed—an effect that depends on the flow setup. At the onset of mean-streamline curvature, an adverse pressure gradient is established and the opposite effect takes place at the end of the curved section. Top walls can be contoured to isolate curvature effects from streamwise pressure gradient (Barlow & Johnston 1988a,b), but in practical configurations the pressure gradient is present and impacts the behaviour of the flow on the curved wall.

A related configuration is the flow in an ‘S’-shaped duct, where the boundary layer is subject to pressure gradients and curvature. Experiments show that the skin friction has local extrema after curvature changes, which are concomitant with streamwise pressure variations (Bandyopadhyay & Ahmed 1993). Corresponding LES by Lopes *et al.* (2006) shows that the mean flow was separated near the convex-to-concave transition due to the strong adverse pressure gradient. Intermittent separation was also observed as the flow progressed from the convex to flat region, but the phenomenon was seldom observed in the flat-to-concave transition (Lopes *et al.* 2006).

Studies that have examined FST-TBL interactions over curved walls have mainly focused on the flow recovery from the curved section on the downstream flat wall. (Kestoras & Simon 1995) compared the boundary layers at low and high inlet free-stream turbulence intensities,  $Tu = 0.6\%$  and  $8\%$ , and reported an increase in skin friction by up to  $20\%$  in the latter case. The authors also contrasted their ability to identify the Görtler vortices in the first case but not in presence of free-stream forcing, which is unlike the established observation that free-stream forcing promotes the generation of outer large-scale motions in flat-plate boundary layers (e.g. You & Zaki 2019). In the same experimental configuration, Kestoras & Simon (1998) used the temperature field over the constant heat-flux plate in order to evaluate the probability of observing boundary-layer

fluid, which was their definition of intermittency. The forced case exhibited enhanced mixing, a trend that is in agreement with flat-plate boundary layers exposed to free-stream turbulence (Hancock & Bradshaw 1989). Their intermittency curves were not however presented in viscous scaling, so it is not possible to quantify the extent to which the free-stream fluid penetrated towards the wall.

### 1.2. Effects of free-stream turbulence on flat-plate turbulent boundary layers

The influence of FST on TBL has much more commonly been studied in zero-pressure-gradient, flat-plate boundary layers. Early experiments were performed using grid-generated FST with intensities  $Tu \lesssim 7\%$  (Simonich & Bradshaw 1978; Hancock & Bradshaw 1983, 1989; Castro 1984). Simonich & Bradshaw (1978) reported that the drag and also the heat-transfer rate increase proportionally to the  $Tu$ . Hancock & Bradshaw (1983) demonstrated a marked effect of the free-stream turbulence lengthscale on TBL response. They introduced the non-dimensional parameter  $b \equiv Tu(\%)/(L_u/\delta + 2)$ , where  $L_u$  and  $\delta$  are the dissipation length scale and boundary layer thickness, and showed that skin friction increases with  $b$ . Hancock & Bradshaw (1989) thermally ‘tagged’ the boundary-layer fluid in order to perform conditional sampling. They reported that FST increases the standard deviation of the intermittency profiles, and that the isotropy of FST reduces the Reynolds-shear-stress correlation coefficient in the boundary layer. Ames & Moffat (1990) and Thole & Bogard (1995, 1996) investigated the influence of higher free-stream intensities  $Tu \gtrsim 10\%$ . The former effort reported that under these intense conditions, skin friction depends not only on  $b$ , but also on the Reynolds number. In contrast, Thole & Bogard (1995) affirmed that the skin friction depends mainly on  $b$ , up to the turbulent intensity  $Tu = 28\%$ . Based on simulations of forced temporal boundary layers, Kozul *et al.* (2020) reported that another relevant parameter is the ratio of eddy-turnover timescales of the free-stream turbulence and boundary layer. Too small a value leads to weak interactions since the external turbulence decays quickly and cannot influence of the boundary layer.

The changes in the spectra and flow structures in the boundary layer, when exposed to free-stream forcing, are noteworthy. Absent free-stream disturbances, a peak in the pre-multiplied energy spectra in the outer part of the boundary layer signals the formation of large-scale motions (Hutchins & Marusic 2007; Mathis *et al.* 2009)—a behaviour that is observed at Reynolds numbers  $Re_\tau \geq 2000$ . Under the influence of FST, that outer peak is observed at lower Reynolds numbers, in both the streamwise and spanwise energy spectra (Thole & Bogard 1996; You & Zaki 2019).

Free-stream turbulence forcing also leads to an increase in the near-wall streamwise velocity fluctuations. Using a scale-decomposition analysis, Dogan *et al.* (2016) attributed this increase to large scales relative to a cutoff wavelength between  $1-2\delta$ . Hearst *et al.* (2018) divided the spectrogram of the streamwise velocity fluctuations into four regions based on the wall-normal height and wavelength. Near the wall, the large-wavelength region is significantly affected by the free-stream turbulence, although the small-scale inner peak was relatively insensitive to external forcing. Based on these results, Hearst *et al.* (2018) concluded that the FST is directly observed in the near-wall region.

The recent direct numerical simulations by You & Zaki (2019, 2020) provided a detailed analysis of the interaction of free-stream turbulence with underlying flat-plate boundary layers at Reynolds numbers exceeding  $Re_\theta \simeq 3200$ . A levelset approach was embedded in the simulations to objectively distinguish the free-stream and boundary-layer fluids, and to quantify the degree of penetration of the former into the later (and vice versa). The levelset approach thus provided an unambiguous description of the respective roles of the free-stream and boundary-layer turbulence, and their respective contributions

to observations through conditional sampling. The results showed that only the low-frequency component of the FST penetrates the logarithmic layer, which is consistent with the phenomenon of shear sheltering (Hunt & Durbin 1999; Zaki & Saha 2009). The outcomes are a direct increase in the turbulence energy in this region, and the formation of large-scale motions at lower Reynolds numbers than in canonical unforced boundary layers. In contrast to the logarithmic region, the FST did not directly reach the buffer layer and the increase in the near-wall TKE was due to an indirect effect: The formation and amplification of the outer large-scale motions modulated the near-wall structures and led to the increase in their turbulence energy.

In contrast to the recent discoveries in context of FST interactions with flat-plate boundary layers, much less is known regarding how such interaction unfolds on curved walls. The present work will highlight that free-stream turbulence has important implications as early as the onset of curvature where the flow experiences an adverse pressure gradient, which can lead to intermittent separation. The external forcing also appreciably alters the boundary-layer statistics and the Görtler structures on the curved section and has important practical implications on the wall stress. We perform two simulations: (i) a reference case with a quiescent free stream and (ii) a forced case with 10% free-stream turbulence intensity at the inlet plane. The setup of the simulations is described in section 2. Key statistical results are presented in section 3 and changes to boundary-layer structures are discussed in section 4. The conclusions are provided in the final section.

## 2. Simulation setup

The flow configuration adopted in the present study is shown in figure 1. The flow is governed by the incompressible Navier-Stokes and continuity equations which, expressed in non-dimensional form, are

$$\frac{\partial u_i}{\partial t} + \frac{\partial u_i u_j}{\partial x_j} = -\frac{\partial p}{\partial x_i} + \frac{1}{Re_{\theta_{in}}} \frac{\partial^2 u_i}{\partial x_j^2} \quad (2.1)$$

$$\frac{\partial u_j}{\partial x_j} = 0. \quad (2.2)$$

The reference scales are the free-stream velocity  $U_\infty$  and the boundary-layer momentum thickness  $\theta_{in}$  at the inflow of the main simulation domain. The momentum-thickness Reynolds number at the inflow is  $Re_{\theta_{in}} \equiv \rho U_\infty \theta_{in} / \mu = 1200$ , where  $\rho$  and  $\mu$  are the density and dynamic viscosity, respectively. The velocity components in the streamwise ( $\xi$ ), wall-normal ( $\eta$ ) and spanwise ( $z$ ) directions are  $u_\xi$ ,  $u_\eta$  and  $w$ , respectively, and the pressure is  $p$ . Note that  $x$  and  $y$  indicate the horizontal and vertical Cartesian coordinates.

The flow equations are solved using a fractional step algorithm on a staggered grid with a local volume-flux formulation (Rosenfeld *et al.* 1991). The algorithm was extensively validated and adopted in DNS of transitional (Schrader *et al.* 2011; Zaki *et al.* 2010) and turbulent flows (Jelly *et al.* 2014; Wang *et al.* 2019). The viscous terms are integrated in time using the implicit Crank–Nicolson method, and the convective terms are treated explicitly using the Adams–Bashforth scheme. The pressure equation is solved using Fourier transform in the periodic spanwise direction and geometric multigrid for the resulting Helmholtz equation, then used to project the intermediate velocity onto a divergence-free field.

Two main simulations are contrasted: a reference (REF) case where the curved-wall boundary layer develops beneath a quiescent free stream and a forced (FRC) case where the free stream is turbulent. In both cases, the flow domains include an initial flat section

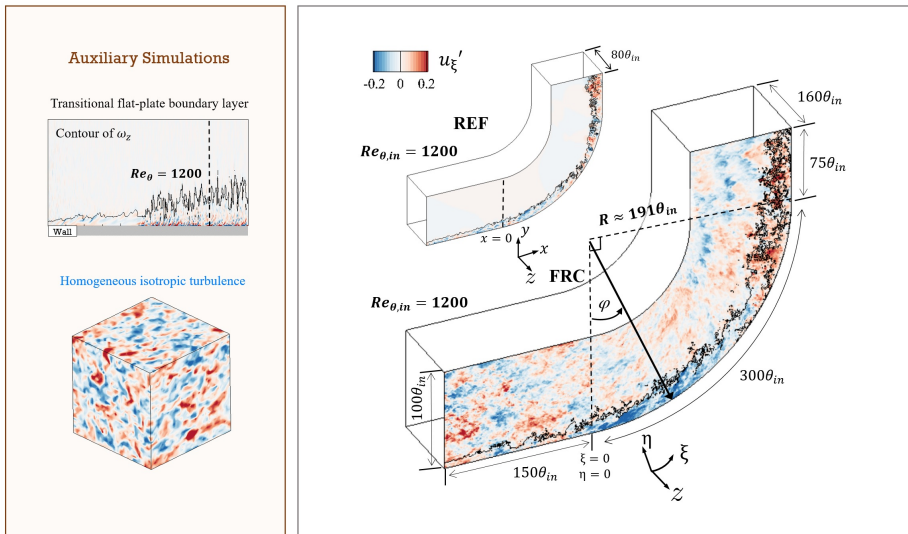


FIGURE 1. Configurations of two auxiliary computations to generate the inflow conditions, and the two main computations of turbulent boundary layer over curved wall without and with free-stream turbulence.

Designation	Inflow	Domain size ( $\theta_{in}$ ) $L_\xi \times L_\eta \times L_z$	No. of grid points $N_\xi \times N_\eta \times N_z$	Resolution $\Delta\xi^+, \Delta\eta^+, \Delta z^+, \Delta t^+$
REF	TBL	$525 \times 100 \times 80$	$2688 \times 896 \times 768$	10.5, 0.29-7.8, 5.6, 0.048
FRC	TBL+HIT	$525 \times 100 \times 160$	$2688 \times 896 \times 1536$	10.5, 0.29-7.8, 5.6, 0.041

TABLE 1. Computational domain sizes, and spatial and temporal resolutions at the inflow plane expressed in viscous ‘+’ units.

( $150\theta_{in}$ ), a curved section ( $300\theta_{in}$ ), and a recovery flat section ( $75\theta_{in}$ ). The quarter-circular section has radius  $R = 191\theta_{in}$ . The spanwise domain of the forced configuration is two times larger than the reference case, in order to accommodate the formation of large-scale structures which are anticipated based on earlier studies (You & Zaki 2019). In addition, the spanwise two-point velocity correlations were evaluated and confirmed that the widths of the domains are sufficiently large. Table 1 summarizes the domain sizes and grid resolutions. The grids are uniform in the span and stretched in the wall-normal direction using a hyperbolic tangent function. In the streamwise direction, the grid spacing is uniform on the bottom wall ( $\eta = 0$ ). On the top surface, the grid is uniform on the curved section and is adjusted smoothly near the changes in curvature. An elliptic grid generation technique (e.g. Thompson *et al.* 1985) is adopted to reduce strong variations in mesh spacing in those regions; the ratio of successive streamwise grid spacing was less than 3%.

No-slip conditions are applied at the bottom wall, while impermeability and no-stress conditions are imposed at the parallel top boundary. The domains are periodic in the spanwise direction, and convective outflow conditions are imposed at the exit planes. In order to seed the inflow TBL and FST in the main computations, two auxiliary

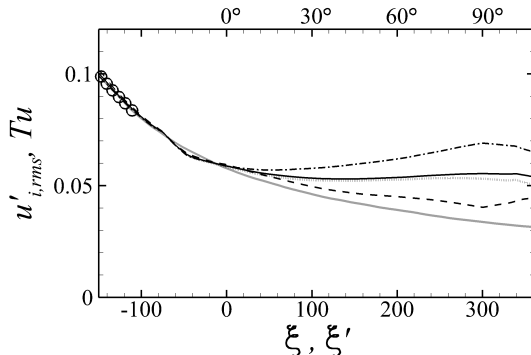


FIGURE 2. Downstream dependence of (black solid line) free-stream turbulence intensity  $Tu$ , (---)  $u'_{\xi,rms}$ , (- · -)  $u'_{\eta,rms}$ , (····)  $u'_{r,rms}$ , and (○) the temporal evolution of  $Tu$  in decaying HIT which exploits the coordinate transformation  $\xi' = U_{\infty}t$ . Gray line indicates the evolution of  $Tu$  on the flat plate (You & Zaki 2019).

simulations are performed and their full details are provided in You & Zaki (2019). The first auxiliary simulation is an independent DNS of transitional flat-plate boundary layer, where a cross-flow plane was stored in the fully turbulent regime at  $Re_{\theta} = 1200$  as a function of time; the same data were used for inflow conditions in a number of studies of TBL (Lee *et al.* 2017; You & Zaki 2019; Motoori & Goto 2019). The second auxiliary simulation is a pseudo-spectral DNS of homogeneous isotropic turbulence (HIT) in a periodic domain with dimensions  $\{L_{\xi}, L_{\eta}, L_z\}_{\text{HIT}} = \{80, 80, 160\}$ , which generates the free-stream turbulence. The inflow HIT has intensity  $Tu = 0.1$  and length scale  $L_k \equiv k^{3/2}/\epsilon \approx 10.8$ , where  $k$  is the turbulent kinetic energy and  $\epsilon$  is the dissipation rate.

At the inflow plane of the main computations, either the time-dependent turbulent boundary layer is applied alone (REF case) or it is superposed with free-stream turbulence (FRC case). In the latter case, the HIT box is introduced above the edge of the boundary layer which was identified using a normalized vorticity threshold,  $\frac{|\omega|}{u_{\tau}^2/\nu} \sqrt{\delta_{99}^+} = 0.2$  where  $\omega$  is the vorticity,  $u_{\tau}$  is the friction velocity,  $\nu$  is the kinematic viscosity and  $\delta_{99}^+$  is the 99% boundary-layer thickness in wall units (Lee *et al.* 2017). A levelset function  $\psi$  is defined at the inflow plane and tags, or differentiates, the fluid within the boundary layer ( $\psi = 1$ ) and the free stream ( $\psi = 0$ ). The transport equation of  $\psi$  is

$$\frac{\partial \psi}{\partial t} + \frac{\partial u_j \psi}{\partial x_j} = 0, \quad (2.3)$$

and therefore  $\psi$  is a diffusion-free scalar that serves as a virtual sharp interface between the two fluids; full details of the implementation and exhaustive validation are provided elsewhere (Jung & Zaki 2015; You & Zaki 2019). The value  $\psi = 0.5$  is adopted as the threshold for conditional sampling of the boundary-layer  $\psi > 0.5$  and free-stream  $\psi < 0$  fluids. Note that the interface height  $\eta_I = \eta(\psi = 0.5)$  provides an objective measure of the boundary-layer thickness that is less sensitive to the details of the profile than the conventional 99% thickness.

Beyond an initial transient and once the flow over the curved surface has reached a statistically stationary state, statistics were collected for  $T_{\text{stat}} = 1,207.5$  (REF) and 892.5 (FRC) convective time units. A bar will indicate an average in homogeneous coordinates, and the prime will refer to perturbation quantities according to Reynolds decomposition, for example  $u_{\xi} = \overline{u_{\xi}} + u'_{\xi}$ .

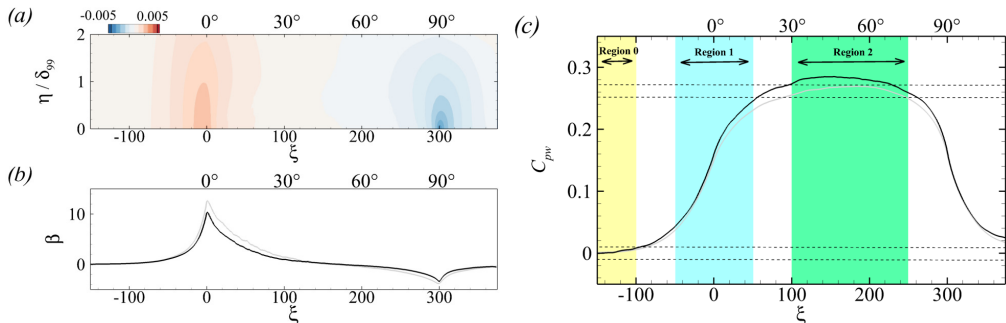
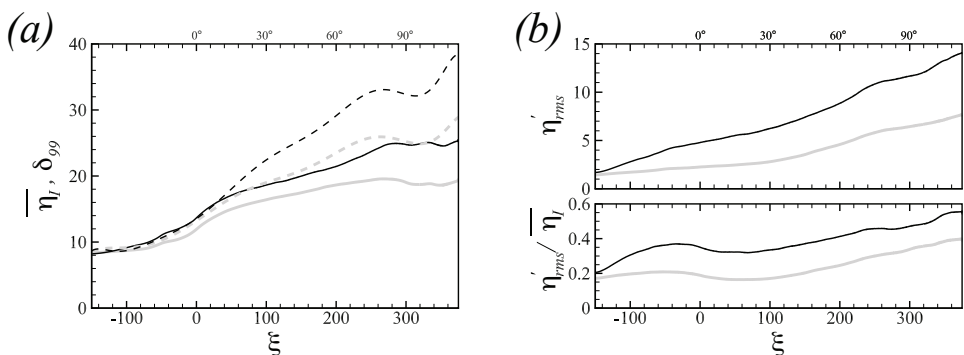
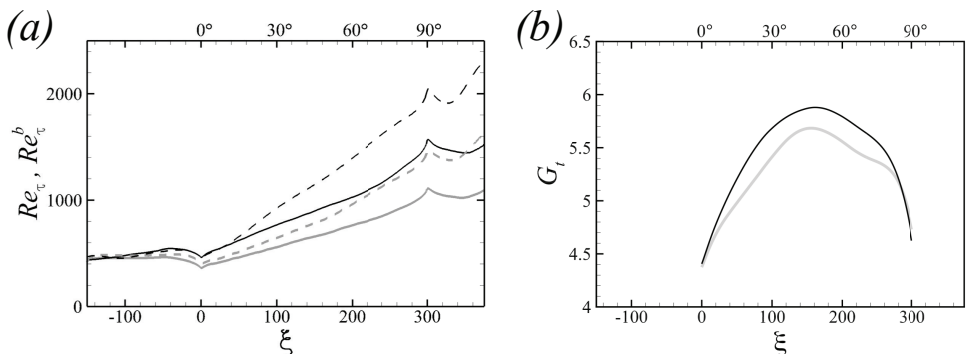


FIGURE 3. (a) Streamwise pressure gradient  $\partial\bar{p}/\partial\xi$  in REF. (b) Clauser pressure-gradient parameter  $\beta$ : (gray) REF and (black) FRC. (c) Wall-pressure coefficient,  $C_{pw}$ : (gray) REF and (black) FRC. Bottom dashed lines indicate ZPG region according to the criterion by Harun *et al.* (2013), and top dashed lines mark  $C_{pw,max} - C_{pw} \leq 0.02$  for REF.

Unlike flat-plate boundary layers, the tangential free-stream velocity on the curved section is not uniform. Instead, it increases linearly outside the boundary-layer edge. That potential velocity profile is denoted  $U_p$ , and is linearly extended into the boundary layer to determine the wall value  $U_{pw}$  (Barlow & Johnston 1988a). The free-stream mean velocity profile influences the development of the FST which we quantify in figure 2. Upstream, within the flat section ( $\xi \lesssim -100$ ), the decay in space in the main simulation agrees with the temporal decay of  $Tu$  in the pseudo-spectral auxiliary DNS of HIT to within the Taylor’s hypothesis  $\xi^* = U_\infty t$ . In that region, the present results also agree with the previous study of free-stream turbulence over a flat-plate boundary layer (You & Zaki 2019), but the two curves show the first signs of dissimilarity ahead of the flat-to-curved transition due to the pressure gradient in that region. Farther downstream, on the curved section, the difference is more pronounced because both the mean shear in the free stream and the strain due to curvature lead to production of Reynolds shear stress, which in turn leads to production of tangential and wall-normal stresses. The outcomes are anisotropy and slower decay and of the free-stream turbulence relative to flow over a flat plate.

Besides the FST input, the wall geometry induces a pressure gradient responsible for turning the oncoming flow, which has profound implications on boundary layer dynamics. Figure 3 shows the streamwise pressure gradient  $\partial\bar{p}/\partial\xi$ , the Clauser parameter  $\beta = \frac{\delta^*}{\bar{\tau}_w} \frac{\partial\bar{p}_e}{\partial\xi}$ , and the wall-pressure coefficient  $C_{pw} \equiv (\bar{p}_{\xi,\eta=0} - \bar{p}_{\xi=0,\eta=0}) / \frac{1}{2}\rho U_\infty^2$ . In the definition of the Clauser parameter,  $\delta^*$  is the displacement thickness,  $\bar{\tau}_w$  is the mean wall shear stress and  $\bar{p}_e$  is the mean pressure at  $\eta = \delta^*$ . Three regions can be clearly delineated: approximately zero-pressure-gradient (ZPG) boundary layer on the flat plate (Region 0), adverse-pressure-gradient (APG) flow near the onset of the curvature (Region 1), and nearly ZPG flow on the concave curve (Region 2). Table 2 provides the information of stations which will be discussed in the following section. Region 0 has been the focus of numerous previous studies of the boundary-layer response to external turbulence (Hancock & Bradshaw 1989; Dogan *et al.* 2016; You & Zaki 2019), and hence the focus herein is directed to Region 1 and Region 2.

Zone	Description	$\xi$	$\varphi$	$Re_{\tau,REF}$	$Re_{\tau,FRC}$
Region 0	ZPG on flat plate	-100	-	455	480
Region 1	APG near onset of curvature	0	0°	363	463
		+50	15°	461	623
Region 2	ZPG on concave curvature	+100	30°	557	769
		+200	60°	762	1027

TABLE 2. Summary of main analysis locations selected based on  $C_{pw}$  in figure 3.FIGURE 4. (a) Downstream development of the (---) boundary-layer thickness  $\delta_{99}$  and (—) mean interface height  $\bar{\eta}_I$  based on levelset function  $\psi = 0.5$ . (b) Downstream development of the root-mean-square fluctuations in the interface height  $\eta'_{rms}$  and its normalized value  $\eta'_{rms}/\bar{\eta}_I$ . (gray) REF; (black) FRC.FIGURE 5. Downstream dependence of (a) the friction Reynolds numbers (—)  $Re_\tau \equiv u_\tau \bar{\eta}_I / \nu$  and (---)  $Re_\tau^b \equiv u_\tau \delta_{99} / \nu$  and (b) Görtler number  $G_t = 43\sqrt{\theta/R}$  (Tani 1962): (gray) REF; (black) FRC.

### 3. Influence of FST on the boundary layer: a statistical perspective

The present simulations involve the combined effects of pressure gradient, curvature and free-stream turbulence on the boundary layer. The outcome is expectedly complex. In this section, we examine the overall changes in the statistical state of the flow.



Free-stream turbulence is known to enhance mixing near the edge of the boundary layer and as a result increases its thickness. Figure 4a reports two quantities that examine this effect: (i)  $\overline{\eta_I} = \overline{\eta(\psi = 0.5)}$  which is the mean height of the virtual interface that distinguishes the boundary layer and the free stream using the levelset function and (ii) the 99% thickness  $\delta_{99}$  defined as the wall-normal location where  $\overline{u_\xi} = 0.99U_p$ . Both thickness metrics increase appreciably near the onset of the curvature due to the adverse pressure gradient. However, over the curve in Region 2, the mean height of the material line  $\overline{\eta_I}$  has a depressed growth relative to  $\delta_{99}$  which is known to be sensitive to details of the mean-velocity profile. Since  $\overline{\eta_I}$  has a physical interpretation, it will be adopted when possible in the rest of this work. The ratio of the boundary-layer thickness to the radius of the curved wall is  $\overline{\eta_I}/R < 0.13$  (and  $\delta_{99}/R < 0.17$ ), which places the present flows in the regime of moderate-curvature effect according to the criterion by Patel & Sotiropoulos (1997).

The root mean square fluctuations in the interface height  $\eta'_{rms}$  and its normalized value  $\eta'_{rms}/\overline{\eta_I}$  are reported in figure 4b. For canonical, unforced flat-plate boundary layers  $\eta'_{rms}/\overline{\eta_I}$  is nearly constant. The present results demonstrate that curvature alone (gray curve,  $\xi \gtrsim 50$ ) promotes the undulation of the interface such that  $\eta'_{rms}/\overline{\eta_I}$  increases along the curved. We therefore expect deep excursions of the free-stream fluid into the boundary layer and vice-versa along the curved section, and free-stream turbulence (black curves) enhances this effect. This view will be reinforced in section 4 where we directly compute intermittency.

The downstream dependence of the friction Reynolds numbers,  $Re_\tau \equiv u_\tau \overline{\eta_I}/\nu$  and  $Re_\tau^b \equiv u_\tau \delta_{99}/\nu$  is plotted in figure 5a. Even though  $\overline{\eta_I}$  and  $\delta_{99}$  increase rapidly near the onset of the curvature, the adverse pressure gradient decreases  $u_\tau$  and the Reynolds numbers. The higher recorded values of  $Re_\tau$  in the FRC case are due in part to the larger boundary-layer thickness, and also an increase in the wall stress in presence of FST. Figure 5b shows the behavior of the Görtler number for the turbulent boundary layers

$$G_t = \frac{U_\infty \theta}{\nu_T} \sqrt{\frac{\theta}{R}} = 43 \sqrt{\frac{\theta}{R}}, \quad (3.1)$$

which uses an eddy viscosity  $\nu_T = 0.0234U_\infty \theta$  (Tani 1962). The definition of the momentum thickness,  $\theta$ , for curved wall flow and associated discussion are provided in Appendix A. Near the onset of curvature, the Görtler number is  $G_t \gtrsim 4$ , which is large enough to promote instability (Smith 1955; Tani 1962), and it is larger in the FRC case. Based on this metric, free-stream turbulence enhances the curvature effects.

Much of the interest in concave-wall boundary layers beneath vortical forcing has been dedicated to the impact on skin friction (Kestoras & Simon 1995, 1998). The probability density function (PDF) of the skin-friction coefficient,  $c_f \equiv \tau_w / \frac{1}{2} \rho U_\infty^2$ , is reported in figure 6, both (a.i) REF and (a.ii) FRC. The later case has a broader PDF which is skewed toward intense  $c_f > 0$  and, as a result, has a larger mean value  $C_f$ . The largest relative increase in  $C_f$  when the flow is forced is on the order of 49%, which is appreciably higher than the 15% observed for the same flow conditions over a flat plate (You & Zaki 2019). Note that the increase is not limited to the low  $C_f$  region near the onset of curvature; instead it is sustained above 40% over the majority of Region 2 on the curved wall. While the effect of forcing appears relatively modest at the onset of curvature, an important change in the state of the flow takes place in that region due to the flow deceleration. As the curvature is approached, the skin friction drops precipitously due to the adverse pressure gradient in both REF and FRC cases. In the latter, FST enhances momentum mixing, which leads to a more moderate reduction of  $C_f$ . The positive values

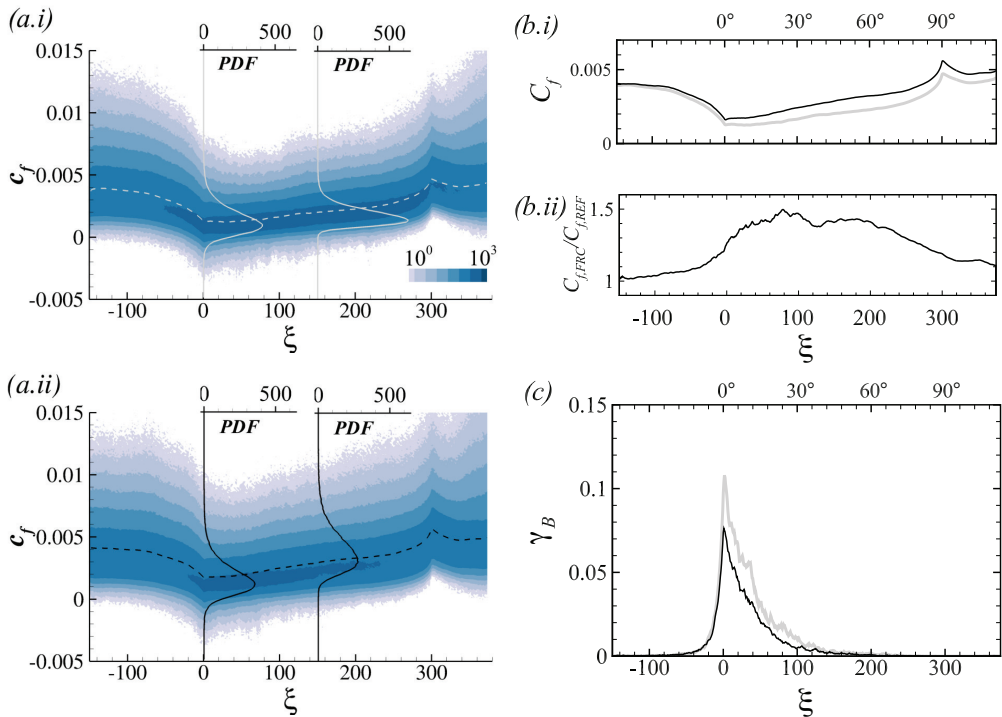


FIGURE 6. (a) Streamwise development of the probability density function (PDF) of instantaneous skin-friction coefficient,  $c_f$ , in (i) REF and (ii) FRC. Dashed lines are the mean values and the solid lines are the PDF at  $\xi = 0$  and  $\xi = 150$ . (b) Downstream dependence of (i) the mean skin-friction coefficient,  $C_f$  and (ii)  $C_{f,FRC}/C_{f,REF}$ . (c) Intermittency of backward flow,  $\gamma_B$ . (Gray) REF; (black) FRC.

of mean  $C_f$  should not, however, mask the intermittent separation clearly captured by  $c_f < 0$  events in figure 6a. The intermittency, or probability, of negative instantaneous wall-shear stress is denoted  $\gamma_B$  and is plotted in figure 6c; its reduced value in FRC is noteworthy due to the qualitative change in boundary layers at separation.

An elegant interpretation of separation is in terms of the spanwise vorticity and its wall flux; the latter is due to the streamwise pressure gradient (Lighthill 1963). Figure 7a shows the spanwise vorticity distribution near the wall. At the onset of curvature, the depletion of negative vorticity is less pronounced in the FRC case, which can be interpreted in terms of a reduction in its mean outflux at the wall. A more detailed view is provided in figure 7b which reports the PDF of instantaneous outflux of negative vorticity at the onset of curvature. The integral of the PDF yields a smaller value for the FRC case, consistent with figure 7a. The PDF of the forced case also has larger positive and negative tails, i.e. stronger instantaneous outflux of negative vorticity (positive values) and also influx (negative values). The former alone would be at odd with reduced frequency of separation. However, the strong influx of negative vorticity (negative values) renders the state of the boundary layer less prone to separation. Intuition may suggest that this effect is associated with enhanced momentum mixing on the flat upstream section, due to the additional vortical motions from the free stream that may breach the boundary layer. However, recent results for flat-plate flows showed that free-stream turbulence does not reach the buffer layer within such short streamwise distance. Instead, the external forcing has an indirect effect of modulation of the near-wall region that enhances the near-wall

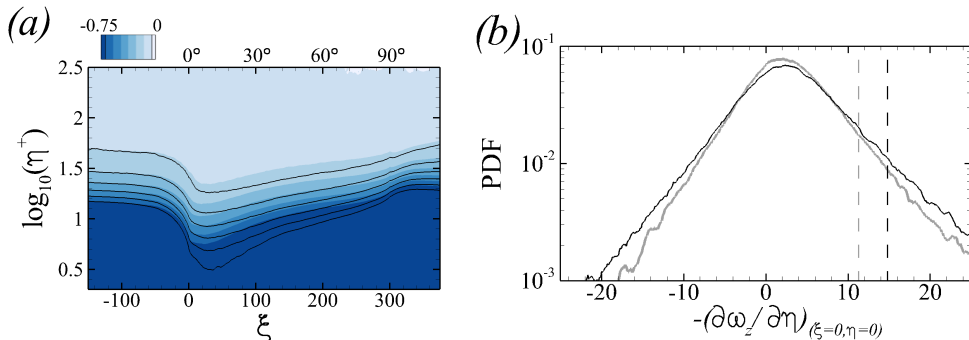


FIGURE 7. (a) Mean spanwise vorticity  $-0.75 \leq \overline{\omega_z} \leq 0$  of (lines) REF and (color) FRC cases. (b) PDF of  $-\partial\omega_z/\partial\eta$  at the wall at the onset of the curvature,  $(\xi, \eta) = (0, 0)$ . Dashed lines mark thresholds for higher amplitude events having the same probability as intermittent separation. (Gray) REF and (black) FRC.

turbulent shear stresses (You & Zaki 2019). The resulting energetic near-wall flow is then less prone to separation at the onset of curvature. Two vertical lines are marked on figure 7b; events with higher amplitudes than these thresholds have the same probability as separation (9.73% for REF and 7.39% for FRC). Based on this simple conceptual model, the results indicate that the threshold required for the forced boundary layer to undergo local intermittent separation is approximately 30% higher than REF. The mean-flow profile  $\overline{u_\xi}$  is therefore anticipated to be fuller in the forced flow, and is shown in figure 8. Indeed, at  $\xi = 0$  through  $\xi = 50$ , the near-wall region of the FRC boundary layer carries more momentum than the reference case.

The change in the mean profile as the flow traverses from the APG Region 1 to the ZPG Region 2 on the curve is noteworthy (figure 8): The figure shows that the mean shear in (b.ii) is slightly reduced in the outer portion of the BL and the mean profile becomes fuller, which is indicative of enhanced mixing due to the free-stream turbulence.

Evidence of persistent, or statistically relevant, Görtler structures is sought by plotting the turbulence stresses in figure 9(a, b), for both the quiescent and turbulent free stream cases. The colour contours show the tangential component, and the lines show the (black) wall-normal and (gray) spanwise ones. The first observation is a sudden change in the contours of  $\overline{u'_\xi u'_\xi}$  across the onset of curvature: The upstream wall-normal profile of  $\overline{u'_\xi u'_\xi}$  has only one maximum in the buffer layer, but beyond  $\xi = 0$  two maxima can be detected: The inner peak retains its original height within the buffer layer  $\eta^+ \approx 11$ , decays quickly due to adverse pressure gradient, and shows faster recovery in the forced flow; In contrast the outer peak is in the logarithmic layer and shifts away from the wall with the downstream growth of the boundary layer. The emergence of the outer peak at that onset of curvature is consistent with APG (see e.g. Hickel & Adams 2008), which is sufficiently large to induce intermittent separation. In addition, relative to the reference case, free-stream turbulence enhances the intensity of these structures—an effect that is anticipated based on previous studies of forced flat-plate boundary layers.

Observations in connection with the tangential stress are not, however, the most important to note from this figure if interest is in the Görtler structures. Instead, attention is drawn to the wall-normal  $\overline{u'_\eta u'_\eta}$  and spanwise  $\overline{w'w'}$  stresses in Region 2. Both stresses amplify on the curved wall, which is consistent with earlier studies (Barlow & Johnston 1988a; Lund & Moin 1996; Arolla & Durbin 2015), and the present results show that the effect of free-stream forcing is rather pronounced. In the lower panels (a.ii and b.ii), the wall-normal coordinate is normalized by the inlet boundary-layer momentum

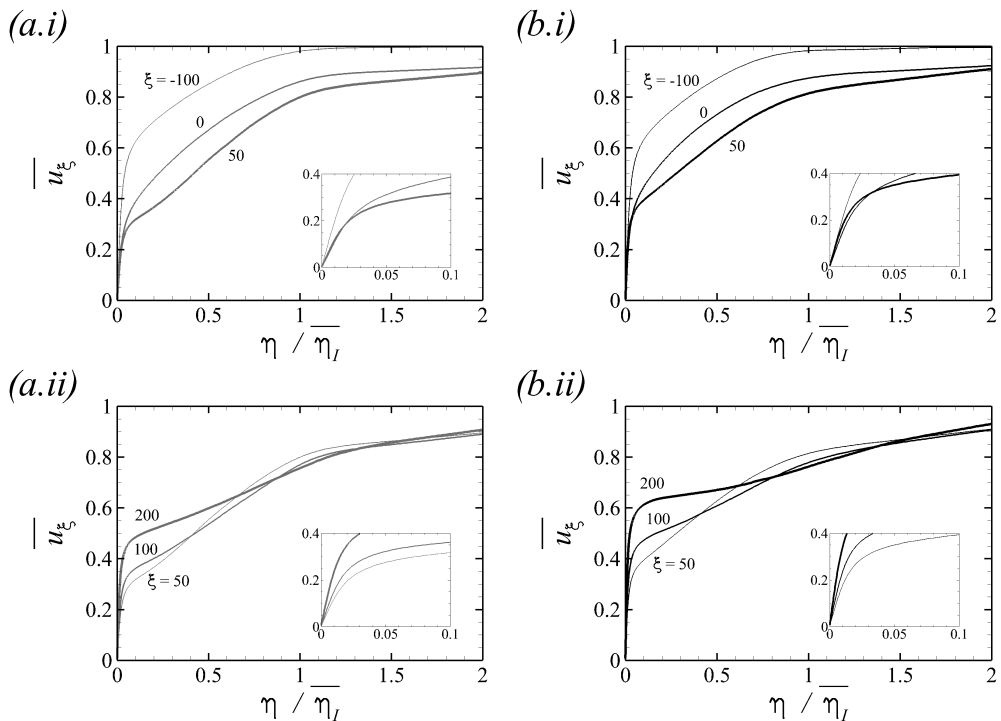


FIGURE 8. Downstream development of the mean streamwise velocity in (a) REF and (b) FRC. (i) Progression from the flat-plate ZPG Region 0 to APG Region 1, and (ii) from APG Region 1 to ZPG Region 2 along the curve.

thickness, which highlights that the separation between the peak  $\overline{u'_\eta u'_\eta}$  and  $\overline{w'w'}$  increases downstream. We interpret the increase in  $\overline{u'_\eta u'_\eta}$  and  $\overline{w'w'}$  as the first, perhaps indirect evidence of Görtler structures (further evidence provided in §4). In reality, instantaneous structures may form at various heights in the boundary layer, meander, decay or be overtaken by other structures. For these reasons, in the statistical interpretation, we regard the peaks of  $\overline{u'_\eta u'_\eta}$  and  $\overline{w'w'}$  as only indicative of the locations of the Görtler structures, and hence the separation distance  $d = \arg \max [u'_\eta u'_\eta(\eta)] - \arg \max [w'w'(\eta)]$  between their peaks as indicative of the size of the vortices (see figures 9*a.ii* and *b.ii*). Figure 10 shows the increase of that size  $d$  with downstream distance, more so in the forced flow in light of the stronger amplification of the outer large-scale structures and the faster growth of the boundary layer.

The departure from isotropy  $I = \frac{u'_\xi u'_\xi}{2k} - \frac{1}{3}$  succinctly captures the changes of the perturbation field within the boundary layer, across the onset of curvature and on the curved wall. Figure 11 shows positive values of  $I$  in the initial flat section, which are consistent with the streamwise Reynolds stress being dominant in flat-plate boundary layers. Note that near the BL edge, (b) shows that mixing with isotropic free-stream turbulence reduces  $I$ . At the onset of curvature, the appreciable increase in  $I$  reflects the increase in  $\overline{u'_\xi u'_\xi}$  in the logarithmic layer (see figures 9*a.i* and *b.i*). Along the curved section,  $I$  decreases with the amplification of  $\overline{u'_\eta u'_\eta}$  and  $\overline{w'w'}$  associated with the formation of outer Görtler structures. The decay in  $I$  is more precipitous in the forced flow in the region  $50 \lesssim \xi \lesssim 300$ , which is symptomatic of the larger amplification of these structures.

The changes in the normal stresses are paralleled by changes in the production of

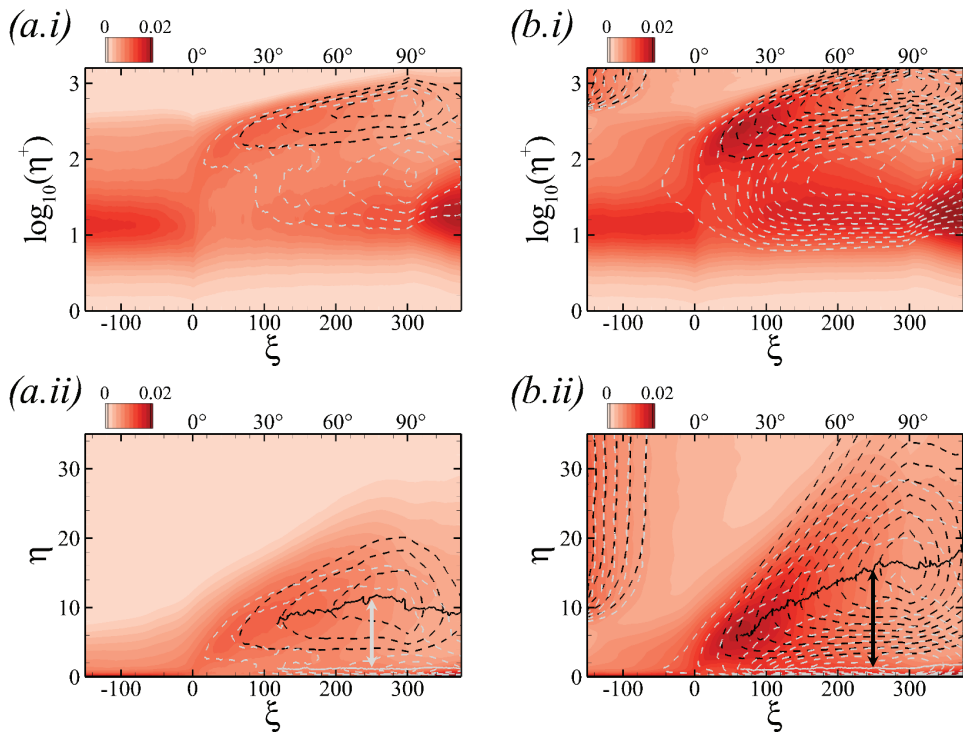


FIGURE 9. Reynolds normal stresses for (a) REF and (b) FRC. The wall-normal coordinate is normalized using (i) viscous and (ii) outer scales. Colours correspond to the streamwise stress, and lines show the (black) wall-normal  $\overline{u'_\eta u'_\eta}$  and (gray) spanwise  $\overline{w'w'}$  stresses, from  $5 \times 10^{-3}$  with increment  $1 \times 10^{-3}$ .

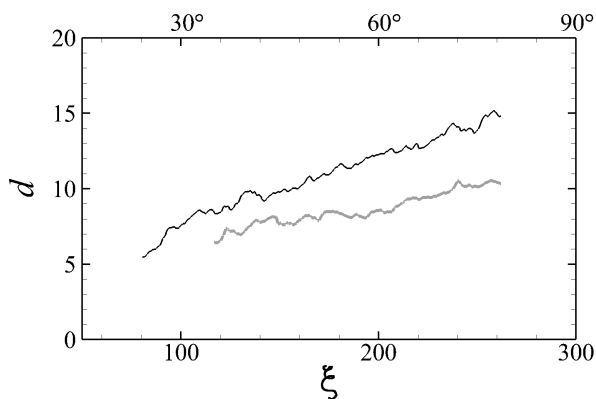


FIGURE 10. Separation distance  $d$  between the peaks of  $\overline{u'_\eta u'_\eta}$  and  $\overline{w'w'}$ . (Gray) REF and (black) FRC.

turbulence kinetic energy,  $\mathcal{P} = -\mathbf{R} : \nabla \mathbf{u}$  where  $\mathbf{R}$  is the Reynolds stress tensor. In figure 12, since a logarithmic scale is adopted in the wall-normal direction, the contours show the pre-multiplied quantity  $\eta^+ \mathcal{P}$  in order to reflect the contribution to the wall-normal integral. Also note that two contour levels are adopted in each figure, with larger range for the outer region of the boundary layer above the curved surface. On the flat upstream

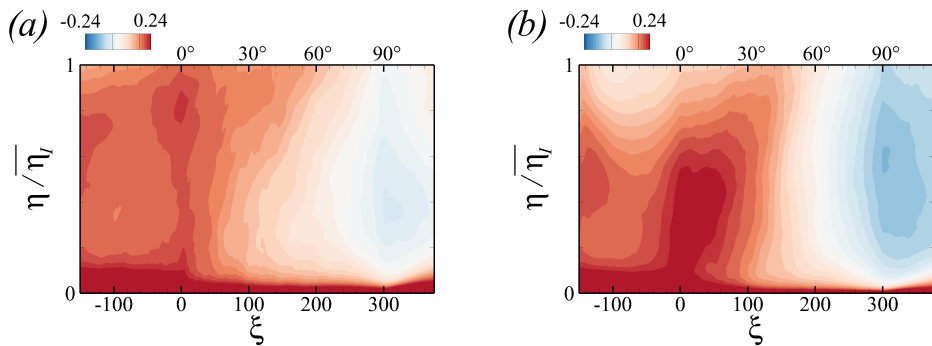


FIGURE 11. Deviation of Reynolds normal stresses from isotropy,  $I = \overline{u'_\xi u'_\xi} / 2k - \frac{1}{3}$ . (a) REF and (b) FRC.

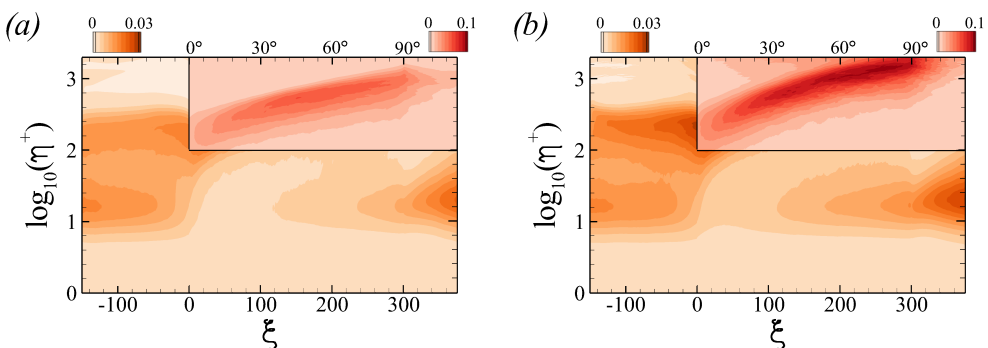


FIGURE 12. Contours of pre-multiplied turbulence kinetic-energy production,  $\eta^+ \mathcal{P}$ . (a) REF and (b) FRC.

section, the inner and outer peaks make comparable contributions to the integrated production, and both are enhanced by free-stream turbulence—an effect that has been detailed in previous studies (You & Zaki 2019). The adverse pressure gradient at the flat-to-curved transition suppresses the near-wall production, and recovery is slow on the curved region albeit faster in presence of free-stream turbulence. In the outer region of the curved-wall boundary layer ( $\xi \gtrsim 0$ ), the production peak is significantly enhanced. While its initial amplification near the onset of curvature coincides with the lifting of near-wall streaks due to APG, its continued amplification downstream coincides with the amplification of the outer stresses and potentially the formation and amplification of Görtler structures. In presence of free-stream forcing, the magnitude of that outer peak is nearly twice its value in the reference configuration.

The TKE production in the outer region is significantly affected by Reynolds shear stresses. We first recall results from forced flat-plate boundary layers for comparison: Even when the free-stream turbulence is isotropic, and hence free of average shear stress, it enhances  $-\overline{u'_\xi u'_\eta}$  within the boundary layer although it reduces the stress correlation coefficient  $r_{u'_\xi u'_\eta} \equiv -\overline{u'_\xi u'_\eta} / u'_{\xi, rms} u'_{\eta, rms}$  (Hancock & Bradshaw 1989; Thole & Bogard 1996). The shear stress and its correlation coefficient for the present curved-wall boundary layers are reported in figure 13. The former quantity is plotted throughout the boundary layer, and the latter is extracted at select locations. Over the curved section,  $-\overline{u'_\xi u'_\eta}$  increases appreciably and reaches larger values for the FRC case. Figure 13b shows the correlation coefficient at  $\eta^+ = 10$  and at the wall-normal height where it is maximum.

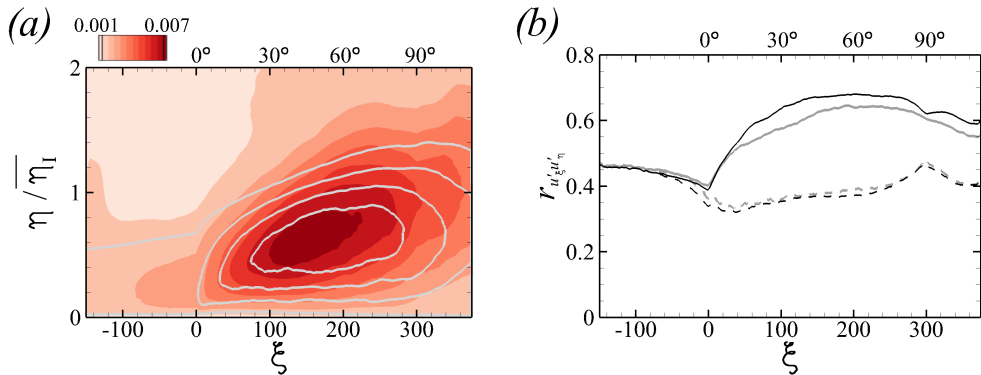


FIGURE 13. (a) Reynolds shear stress  $-\overline{u'_\xi u'_\eta}$  for (line) REF and (color) FRC cases. Contours lines correspond to levels from  $1 \times 10^{-3}$  with increment  $1 \times 10^{-3}$ . (b) Downstream development of shear-stress correlation coefficient  $r_{u'_\xi u'_\eta}$ , extracted at (---)  $\eta^+ = 10$  and (—) wall-normal location of the maximum. (Gray) REF and (black) FRC.

The figure shows that the peak occurs at  $\eta^+ = 10$  on the flat section of the wall, but the correlation at that location decays due to the pressure gradient (Gungor *et al.* 2016). Note that this effect was not reported in the previous experimental curved-wall studies by Barlow & Johnston (1988a) who removed the effect of pressure gradient by contouring the top convex wall. On the curved wall, however, the peak shifts higher in the boundary layer and is much larger in magnitude due to the coherence of the turbulence structures in that region. In addition, the coefficient of the forced case is markedly greater in the outer region than that of the reference flow. We anticipate that the FST strengthens the outer roll motion on the curved region, thereby enhancing the correlation coefficient.

This section has demonstrated that the free-stream turbulent forcing mitigates the intermittent separation that can take place at the onset of curvature, enhances mixing of mean momentum along the curved wall and leads to appreciable and sustained increase in skin friction. The forcing also alters the state of the turbulence within the boundary layer along the curved wall. The distribution of the turbulent stresses suggests the formation of naturally triggered Görtler structures, which are more energetic and larger in size when the boundary layer is buffeted by the external turbulence. The following section upholds these interpretations by directly probing the flow structures on the curved wall without and with FST.

#### 4. Modification of boundary-layer structures

A commonly adopted approach to identifying coherent vortical motions is to evaluate an invariant of the velocity gradient tensor, for example  $Q \equiv \Omega_{ij}\Omega_{ij} - S_{ij}S_{ij}$  where  $S_{ij}$  is the symmetric, rate-of-deformation tensor and  $\Omega_{ij}$  is the anti-symmetric, spin tensor. Figure 14 shows iso-surfaces of the  $Q$ -criterion coloured by their wall-normal distance. In both REF and FRC, the structures grow and spread in  $\eta$  as they travel into the concave curvature; similar observations were made for FST-free flows (Arolla & Durbin 2015). This trend is consistent with the development of the outer peak in the profiles of Reynolds stresses (figures 9). The increase in vortical activity has previously been attributed to Görtler vortices due to the centrifugal effect, although coherent large-scale vortical structures are not apparent in the figure. It is also important to note that the response in presence of FST is hardly distinguishable from the reference flow, based on the

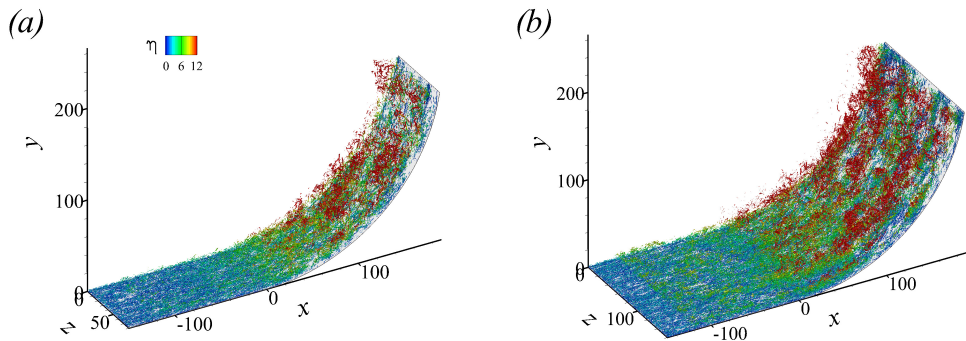


FIGURE 14. Iso-surface of  $Q$ -criterion with threshold  $Q = 0.03$ , coloured by  $0 \leq \eta \leq 12$ . (a) REF and (b) FRC.

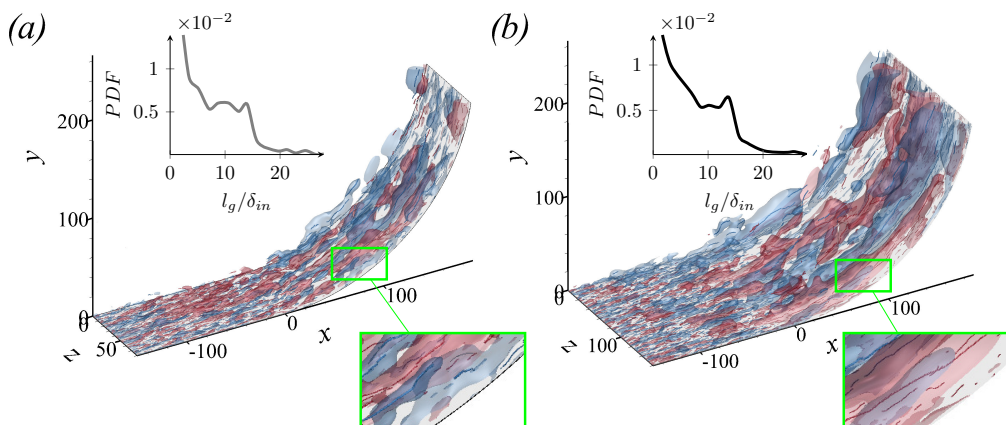


FIGURE 15. Iso-surfaces of filtered streamwise velocity, (red)  $\hat{u}'_{\xi} = +0.06$  and (blue)  $\hat{u}'_{\xi} = -0.06$ . Lines within the transparent surfaces mark the cores of the structures. (a) REF and (b) FRC. Insets show the PDF of the lengths of the cores in the outer region  $30 < \eta^+ < \eta^+_I$  and which cross  $\xi = 100$  ( $\varphi = 30^\circ$ ).

instantaneous  $Q$  iso-surfaces. While streamwise organization is visually discernible in the figure, Görtler vortices which are associated with coherent longitudinal roll motions can not be easily identified, and attempts to adopt filtering techniques were not successful.

Direct identification of naturally emerging Görtler motions in turbulent flows over curved walls is difficult. This challenge led Barlow & Johnston (1988b) to artificially impose them using vortex generators. For streamwise homogeneous flows, Moser & Moin (1987) performed streamwise averaging of the velocity field to visualize vortical structures in a curved channel flow. Due to streamwise inhomogeneity in the present configuration, however, we consider the Gaussian-filtered velocity fields as done in previous studies (Hutchins & Marusic 2007; Lee *et al.* 2014; Hwang *et al.* 2016). The displacement of momentum effected by the Görtler motions generates coherent tangential velocity perturbations that are readily observable in the Gaussian-filtered  $\hat{u}'_{\xi}$ . Following the approach described by Lee *et al.* (2017), we evaluate iso-surfaces of  $\hat{u}'_{\xi}$  and identify the cores of those structures (see figure 15). In order to interpret the present results, it is helpful to recall those for a flat plate at the same Reynolds numbers (You & Zaki 2019): In that case, a canonical boundary layer without free-stream forcing does not develop outer large-scale motions; under free-stream turbulence, large-scale structures



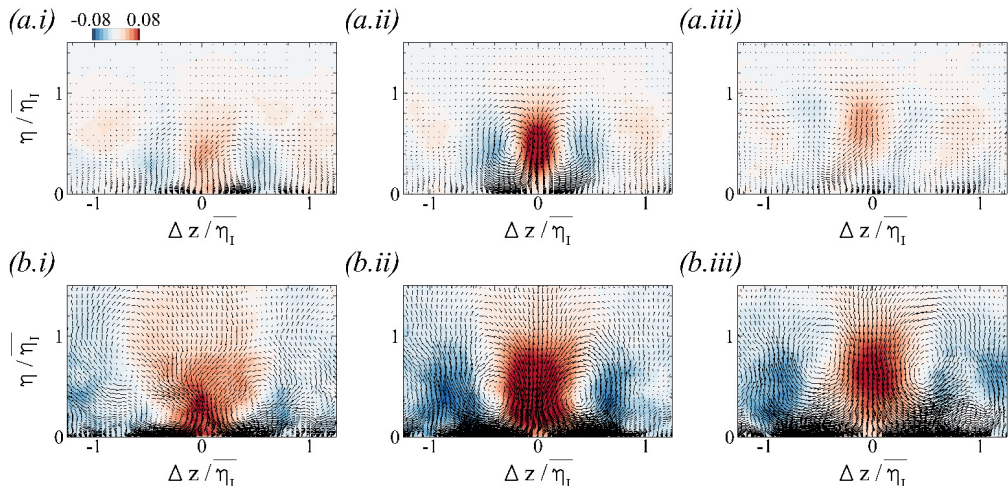


FIGURE 16. Conditionally averaged positive streamwise velocity on the curve with reference position  $\xi_o = 100$  ( $30^\circ$  station), and coloured by  $u'_{\xi_{\mathcal{L}}}^P$ . Black vectors are  $(u'_{\eta_{\mathcal{L}}}^P, w'_{\eta_{\mathcal{L}}}^P)$ . (a) REF, (b) FRC, (i)  $\Delta\xi = -25$ , (ii)  $\Delta\xi = 0$ , and (iii)  $\Delta\xi = +25$ .

form and amplify, but a much longer streamwise extent is required than the flat region in the present configuration. Contrasting REF and FRC for  $\xi < 0$ , the velocity structures appear similar in that region, and hence any differences downstream on the curved wall are due to the interaction in that regime. There, the outer structures are clearly visible, and the iso-surfaces are larger in presence of free-stream forcing which also implies that the tangential velocities within their cores are higher in amplitude.

Figure 15 also shows that we can identify the cores of the large-scale structures, which can be classified into positive  $\mathcal{C}^P$  ( $\hat{u}'_{\xi} > 0$ ) and negative  $\mathcal{C}^N$  ( $\hat{u}'_{\xi} < 0$ ) ones. The PDF of the lengths  $l_g$  of these cores is reported in the inset, for structures that are detected in the outer region  $30 < \eta^+ < \eta_I^+$  at  $\xi = 100$  ( $\varphi = 30^\circ$ ). The PDF shows an increased probability at lengths  $O(5 - 6 \delta_{99})$ . In addition to their streamwise advection, these cores exhibit a weak spanwise drift velocity with equal probability of positive or negative value. The average  $w$  along the core of a structure is typically one order of magnitude less than the local  $w_{\text{rms}}$ .

Definitive evidence of the outer roll, or Görtler, motions and their influence on the near-wall flow are sought by computing conditionally averaged velocity perturbation fields. The condition adopted for averaging is the existence of a core of an outer tangential velocity structure, and is further differentiated into positive and negative ones similar to the instantaneous visualization (c.f. figures 15). The conditionally averaged perturbation fields are therefore,

$$\mathbf{u}_{\mathcal{L}}^P(\Delta\xi, \eta, \Delta z) = \overline{\mathbf{u}(\xi_o + \Delta\xi, \eta, z + \Delta z) \mid \mathcal{C}^P}_{|_{30 < \eta^+ < \eta_I^+}}, \quad (4.1)$$

$$\mathbf{u}_{\mathcal{L}}^N(\Delta\xi, \eta, \Delta z) = \overline{\mathbf{u}(\xi_o + \Delta\xi, \eta, z + \Delta z) \mid \mathcal{C}^N}_{|_{30 < \eta^+ < \eta_I^+}}. \quad (4.2)$$

Figures 16 and 17 show the contours of  $\mathbf{u}_{\mathcal{L}}^P$  and  $\mathbf{u}_{\mathcal{L}}^N$ , with the reference streamwise position  $\xi_o = 100$  ( $30^\circ$  station). Vectors represent the in-plane velocity components. While the outer roll motions are visible at  $\Delta\xi = 0$  in the canonical boundary layer, they are much more pronounced (larger in size and amplitude) beneath free-stream turbulence. The more important observation, however, is the persistence of the roll motion and associated tangential velocity response upstream and downstream of the reference position. In the

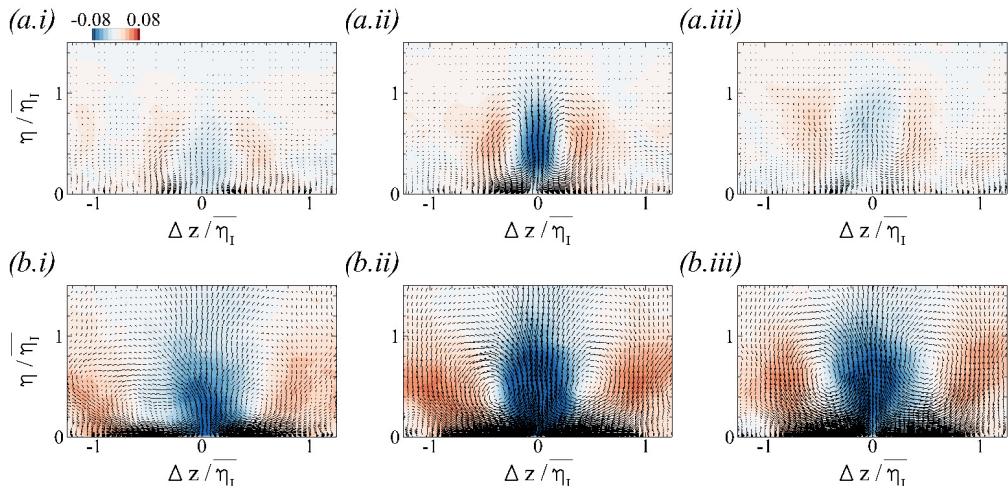


FIGURE 17. Conditionally averaged negative streamwise velocity on the curve with reference position  $\xi_o = 100$  ( $30^\circ$  station), and coloured by  $u'_{\xi_{\mathcal{L}}}^N$ . Black vectors are  $(u'_{\xi_{\mathcal{L}}}^N, w'_{\xi_{\mathcal{L}}}^N)$ . (a) REF, (b) FRC, (i)  $\Delta\xi = -25$ , (ii)  $\Delta\xi = 0$ , and (iii)  $\Delta\xi = +25$ .

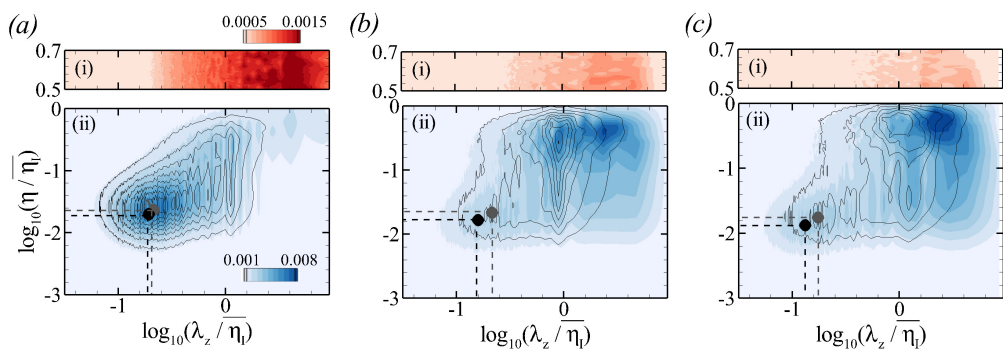


FIGURE 18. Pre-multiplied spanwise energy spectra at (a)  $\xi = -100$ , (b)  $\xi = 50$  and (c)  $\xi = 100$ , with levels (i)  $0.0005 \leq \kappa_z \Phi_{u'_\xi u'_\xi} \leq 0.0015$  in the free stream and (ii)  $0.001 \leq \kappa_z \Phi_{u'_\xi u'_\xi} \leq 0.008$  in the boundary layer. (Black lines) REF and (color) FRC. Filled circles mark  $\eta^+ = 10$  and  $\lambda_z^+ = 100$  in (gray) REF and (black) FRC.

quiescent flow, the perturbation field  $u'_{\xi_{\mathcal{L}}}^{\{P,N\}}(\Delta\xi = \pm 25)$  is decorrelated appreciably from the reference point (e.g. figures 16-17, *a.i* and *a.iii*). In contrast, in the FRC case, the structures identified at the reference location persist beyond  $\Delta\xi = \pm 25$  (e.g. figures 16-17, *b.i* and *b.iii*). The improved coherence underscores that free-stream turbulence does not decorrelate the turbulence within the logarithmic layer on the curved section, but rather promotes it.

The outer roll motion also increases in size with downstream distance, from  $\Delta\xi = -25$  to  $+25$ . This view was also supported by further evidence (not shown) where we evaluated the conditional velocity fields using equations (4.1) and (4.2) at reference locations  $\xi_o = 75$  and  $\xi_o = 125$ . The large roll motions which are growing with downstream distance in the forced flow are consistent with earlier statistical evidence based on the Reynolds stress, namely that the gap between the peak  $\overline{u'_\eta u'_\eta}$  and  $\overline{w' w'}$  increases along the curved wall (c.f. figure 10).

The amplification of Görtler motions depends on the stability characteristics of the

boundary layer and the upstream forcing (Hall 1982). In the REF case, the forcing is provided solely by the turbulence in the upstream boundary layer, and an associated Görtler response develops on the curve. In the FRC case, there is the additional free-stream forcing which interacts with the developing boundary layer. As early as the flat section, the results by You & Zaki (2019) showed that the low-frequency perturbations from the free stream are effective at penetrating the logarithmic layer. The adverse pressure gradient which reduces shear sheltering can promote such penetration (Zaki & Durbin 2006). As a result, the dominant Görtler response on the curved section may differ from the REF case. We evaluate the spectra to examine the energy at different scales in the perturbation fields. Figure 18 shows the spanwise energy spectra of the streamwise velocity,

$$\Phi_{u'_\xi u'_\xi}(\lambda_z) = \int_{-\infty}^{\infty} \overline{u'_\xi(z)u'_\xi(z+\zeta)} e^{-i\kappa_z \zeta} d\zeta, \quad (4.3)$$

pre-multiplied by spanwise wavenumber  $\kappa_z = 2\pi/\lambda_z$  where  $\lambda_z$  is the wavelength. Three streamwise positions are considered, and at each the spectrum is reported (*i*) in the free stream and (*ii*) within the boundary layer where line and colour contours correspond to the REF and FRC case, respectively. On the flat section (figure 18*a*), only an inner peak is visible, be that in the REF or FRC boundary layer. A faint increase of energy is observed near the edge of the FRC boundary layer at large spanwise scales that are commensurate with the most energetic wavelengths in the free stream in (*a.i*). On the curved section, the energy in the small wavelengths decreases (figures 18*b-c*), which is consistent with reduced TKE dissipation (not shown). In the reference flow, a clear outer peak emerges at  $\lambda_z \approx \overline{\eta}$ . In contrast, in FRC at  $15^\circ$  (color contour of figure 18*b*), there are two outer peaks and both are associated with Görtler motions: The first, at the smaller spanwise wavelength (left), coincides with the contours of the canonical boundary layer and is the naturally forming Görtler vortices. The second emerges at the wavelength of the free-stream turbulent forcing (see panel (*a.i*)); this peak is the boundary layer Görtler response to the external forcing. The two peaks ultimately merge downstream  $\xi = 100$ , with the larger Görtler vortices becoming the most dominant. Similar to earlier studies of turbulence on curved walls (Tani 1962), comparison can be made to results from linear stability. In our configuration, at  $\xi = 50$ , the local Görtler number  $G_t = 5.4$  (c.f. figure 5*b*) and the most energetic spanwise wavenumber is  $k_z \theta = 0.43$  which is also the most unstable mode according to linear theory (Smith 1955; Tani 1962). An important observation is the extent to which that wavenumber persists, or remains energetic, deep into the boundary layer, which is suggestive of a stronger modulation of the near-wall region than in flat plates, perhaps even a direct influence.

The small-scale energy in the near-wall region is also modified by the free-stream forcing. Figure 18 shows that, along the curved wall, energy shifts towards smaller spanwise wavenumbers in FRC which is consistent with enhanced dissipation. The inner peak in the spectra is generally located at  $\eta^+ \approx 10$  and  $\lambda_z^+ \approx 100$ , and thus the downstream dependence of  $\kappa_z \Phi_{u'_\xi u'_\xi}$  at the position is provided in figure 19. Downstream of the fast decay associated with the adverse pressure gradient at the onset of curvature,  $\kappa_z \Phi_{u'_\xi u'_\xi}$  recovers at a faster rate for FRC.

The coherent outer Görtler motions have important implications, including their ability to enhance mixing and, in the forced configuration, potentially transport the free-stream turbulence deep into the boundary layer towards the wall. An objective measure of penetration of the free-stream fluid into the boundary layer is the intermittency  $\gamma$ . Starting from the levelset function that provides an objective instantaneous virtual

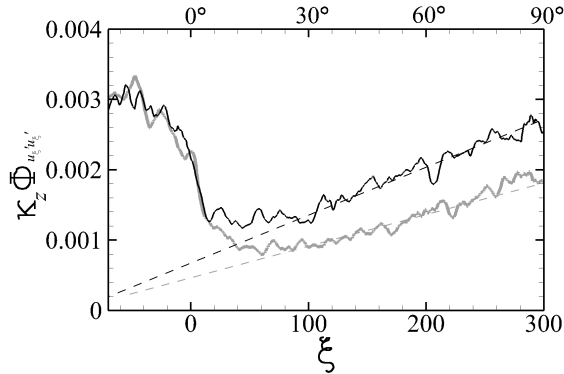


FIGURE 19. Downstream development of  $\kappa_z \Phi_{u'_\xi u'_\xi}$  at  $\eta^+ = 10$  and  $\lambda_z^+ = 100$ : (gray) REF and (black) FRC. Dashed lines indicate the recovery rate in Region 2.

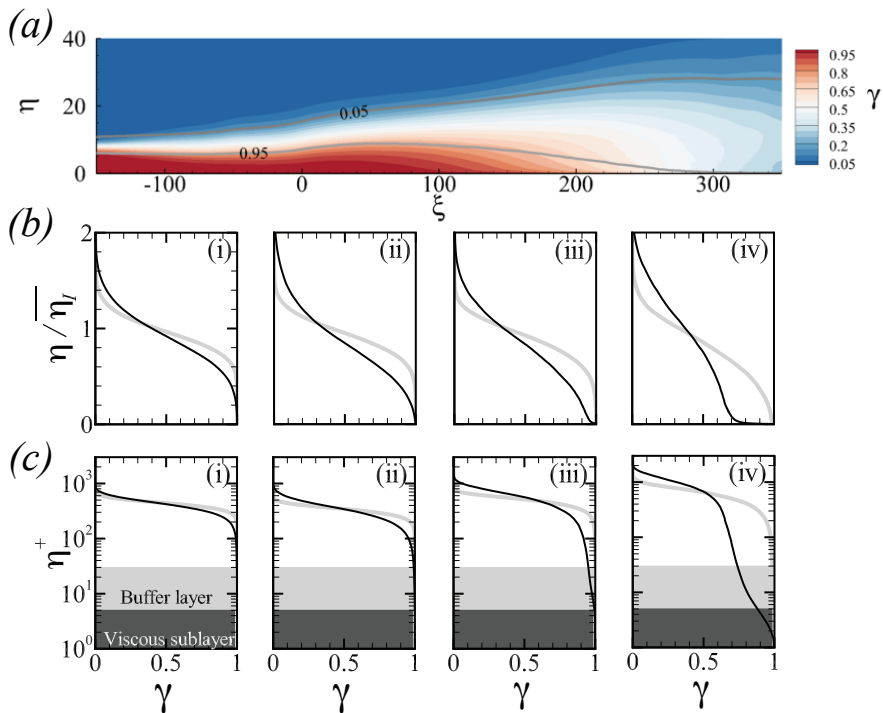


FIGURE 20. (a) Intermittency  $\gamma$  for (lines,  $\gamma = \{0.05, 0.95\}$ ) REF and (colour,  $0.05 \leq \gamma \leq 0.95$ ) FRC. Intermittency profiles in (b) outer and (c) viscous units, at (i-iv)  $\xi = \{-100, 0, 100, 200\}$ ; (Gray) REF and (black) FRC.

interface between the two regions, an indicator function is defined  $\Gamma = \{0, 1\}$  for  $\psi \geq 0.5$ , and then averaged to obtain  $\gamma = \bar{\Gamma}$ . We recall that in a flat-plate boundary layer, You & Zaki (2019) adopted the same measure and demonstrated that the free-stream turbulence does not breach the buffer layer within the streamwise domain length of interest here. The results for the present curved wall configuration are reported in figure 20. Panel (a) captures the difference between the flat and curved sections: even for the unforced flow the intermittency iso-lines spread more quickly on the curve which is indicative of

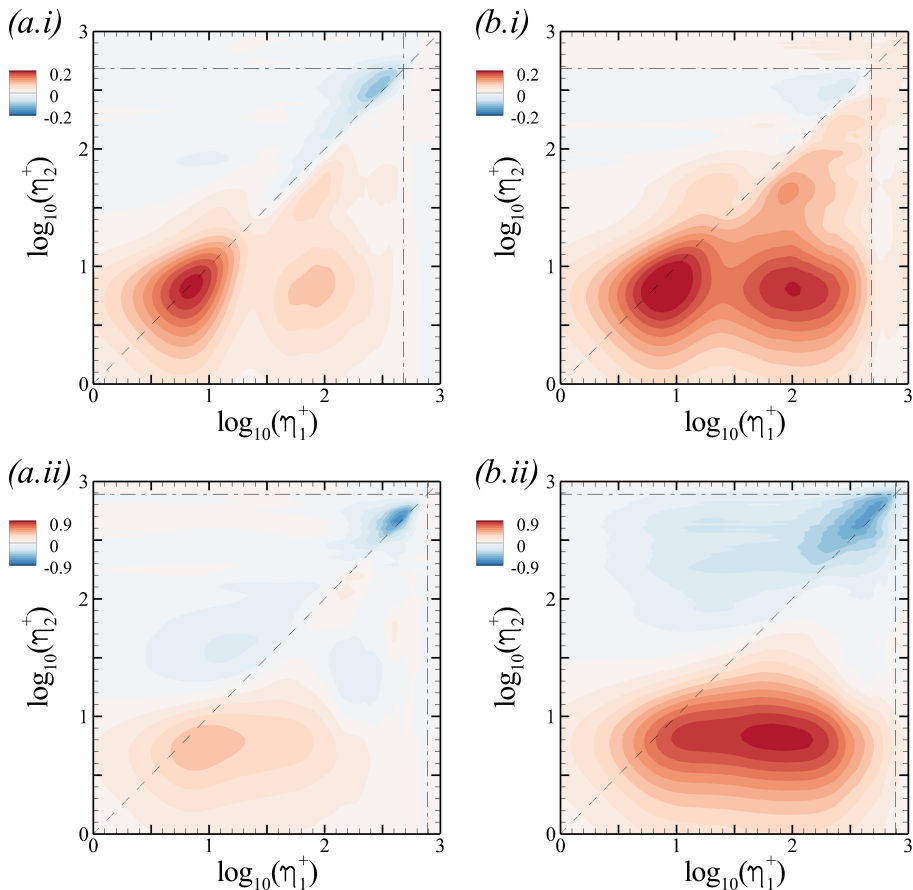


FIGURE 21. Amplitude-modulation coefficient  $C_{u_{\xi}, u_{\xi}}/u_{\tau}^2$  for (a) REF and (b) FRC cases. (i) Flat section ( $\xi = -50$ ) and (ii) curved section ( $\xi = 100$ ;  $30^\circ$  station). Vertical and horizontal dash-dotted lines ( $- \cdot -$ ) mark the edge of the boundary layer,  $\eta = \bar{\eta}_T$ .

enhanced mixing of the free-stream and boundary-layer fluids (see also the wall-normal profiles in outer scaling in panel (b)). Forcing by free-stream turbulence amplifies these trends significantly, and in panels (c.iii-iv) we observe remarkable levels of penetration of free-stream turbulence inside the buffer layer at  $\xi \gtrsim 100$  ( $\varphi > 30^\circ$ , Region 2). This enhanced “mixing” is unique to the present configuration and is precipitated by the large-scale outer roll motions, transporting the free-stream fluid deep towards the wall and ejecting near-wall fluid outwards. The interaction of the outer and inner regions is therefore direct. Ultimately, however, this large-scale effect is also accompanied by further dispersion of the ingested turbulence due to the various flow scales within the boundary layer, and by molecular diffusion acting on the smallest scales. Thus, we next consider the recovery of the near-wall small-scale structures on the curved wall, and in particular their modulation by the outer large scales that can spur that recovery.

Bernardini & Pirozzoli (2011) defined the two-point amplitude modulation (AM) coefficient  $C_{u_{\xi}, u_{\xi}}(\eta_1, \eta_2)$  in order to quantify the influence of the large-scale motion at  $\eta_1$  on the near-wall motion at  $\eta_2$ , where

$$C_{u_{\xi}, u_{\xi}}(\eta_1, \eta_2) = \overline{u_{\xi L}'(\eta_1) u_{\xi EL}'(\eta_2)}, \quad (4.4)$$

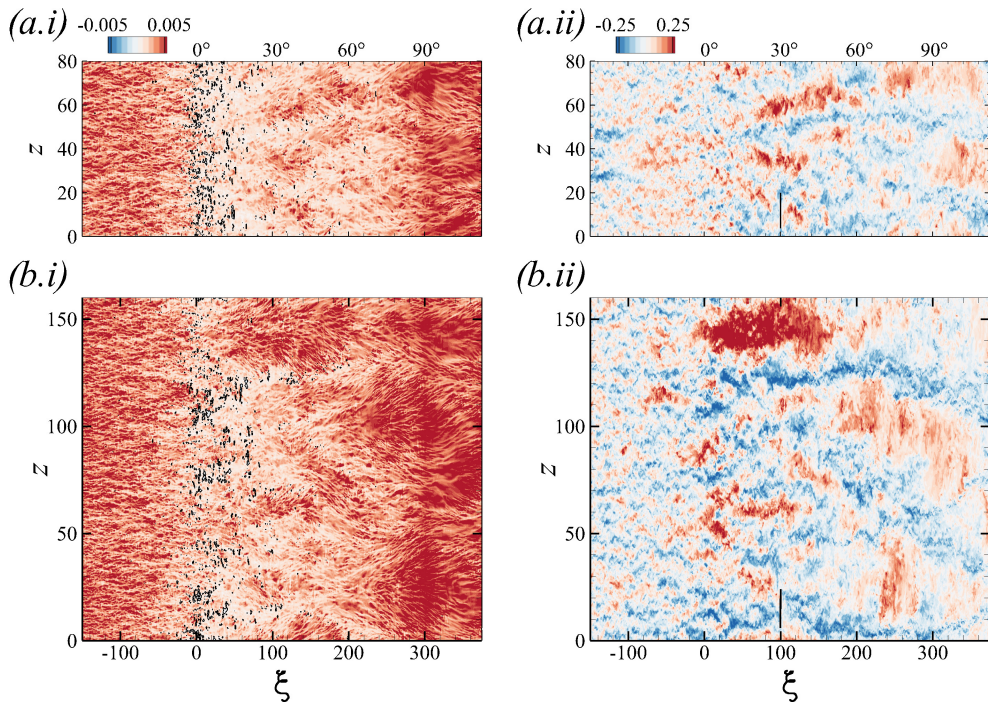


FIGURE 22. (i) Top view of instantaneous skin-friction coefficient,  $-0.005 \leq c_f \leq 0.005$  and black isocontour marks  $c_f = 0$ . (ii) Instantaneous streamwise-velocity fluctuations  $-0.25 \leq u'_\xi \leq 0.25$  at  $\eta \approx 3$  ( $\eta^+ \approx 100$  at  $\xi = 0$ ). (a) REF; (b) FRC. The short black line in (ii) is a graphical length scale equal to  $\overline{\eta}_I$  at  $\xi = 100$ .

$u_{\xi L}'$  is a large-scale velocity, and  $u_{\xi EL}'$  is a filtered envelope of a small-scale part. The cut-off filter for the large- and small-scale signal is set to  $0.5\overline{\eta}_I$ , which from the spectra shown in figure 18 should discriminate these scales. In the flat section ( $\xi = -100$ ), figure 21*i* shows that upstream boundary layer exhibit a weak level of modulation beneath a quiescent free stream, and this effect is enhanced under FST. In the latter case, the outer large-scale motions at  $\eta_1^+ \approx 100$  show relatively higher level of modulation of the small scales at  $\eta_2^+ \approx 7$ . These results are typical of flat plates, and the values of  $C_{u_\xi, u_\xi}(\eta_1, \eta_2)$  would increase downstream if the flat section were extended. A qualitative change takes place over the curved section: Figure 21*ii* highlights a much stronger modulation (note the change in the contour levels), especially in the forced flow where the coefficient at  $(\eta_1^+, \eta_2^+) \approx (100, 7)$  is now the most dominant and is nearly twice as high as without FST. The results for FRC are the outcome of the energetic footprint of the large scales that persists near the wall (figure 18) and leads to a faster recovery of near-wall small scales (see figure 19).

The deep ingestion of outer fluid by the Görtler structures not only modulates the near-wall scales but also influences the stress at the wall which is of practical interest. In order to empirically demonstrate this connection, figure 22*i* shows an instantaneous realization of the skin-friction coefficient  $c_f$ , and panels *ii* show the corresponding tangential velocity fluctuations  $u'_\xi$  in the outer region. The contours of  $c_f$  initially have a streaky pattern that is disrupted by the APG at the onset of curvature. However, the most important observation is downstream, where localized large-scale regions of high

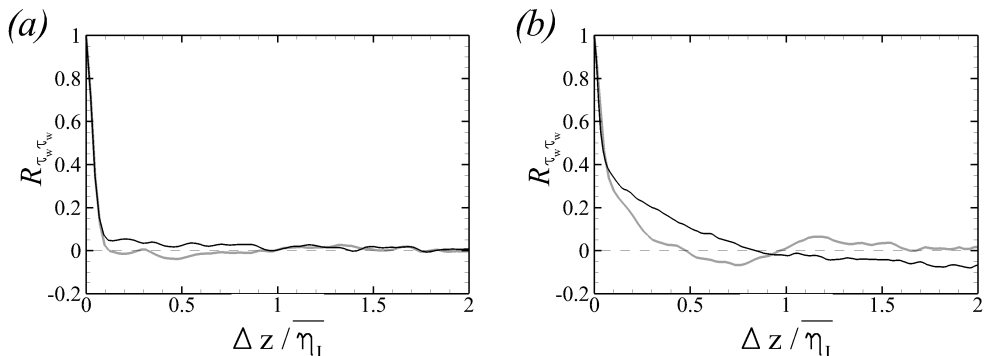


FIGURE 23. Spanwise two-point correlation of the wall-shear stress  $R_{\tau_w \tau_w}$  at (a)  $\xi = -100$  and (b)  $\xi = 100$  ( $30^\circ$  station). (Gray) REF and (black) FRC.

$c_f$  are observed on the curved wall beneath outer large-scale and high-amplitude  $u'_\xi$  perturbations.

Close inspection of figure 22(i) also provides visual support of faster recovery of the small-scale near-wall structures. For both REF and FRC, the streamwise-aligned near-wall streaks have an intense signature in the wall stress on the flat plate, which is abruptly disrupted near the onset of curvature  $\xi \approx 0$ . The re-emergence of this signature across the span is clear near the end of the curved wall,  $\xi \approx 300$ . The key observation, however, is free-stream turbulence re-establishes these streaky structures much earlier upstream on the curve, albeit intermittently, as early as  $\xi \approx 50$  for this particular flow realization.

The above empirical observations are quantified, firstly using the normalized two-point correlation of the wall stress in the span,

$$R_{\tau_w \tau_w}(\xi, \Delta z) = \frac{\overline{\tau_w(\xi, z)\tau_w(\xi, z + \Delta z)}}{\overline{\tau_w(\xi, z)\tau_w(\xi, z)}}. \quad (4.5)$$

Figure 23a shows that, on the flat section ( $\xi = -100$ ), the wall stress  $\tau_w$  decorrelates within a fraction of the boundary layer thickness. In contrast, on the curve, the stress is much more correlated in the span, and the correlation length is much wider in presence of free-stream forcing potentially due to the larger size of the outer Görtler motions.

Here we examine whether the wall stress beneath the outer roll motions is indeed statistically large in scale and magnitude, not only in a single realization as shown in figure 22 but in a statistically significant fashion. This point is upheld by directly evaluation the average perturbation wall stress,

$$c_f^P(\Delta\xi, \Delta z) = \overline{c'_f(\xi + \Delta\xi, z + \Delta z) \mid \mathcal{C}^P_{|30 < \eta^+ < \eta_I^+}} \quad \text{and} \quad (4.6)$$

$$c_f^N(\Delta\xi, \Delta z) = \overline{c'_f(\xi + \Delta\xi, z + \Delta z) \mid \mathcal{C}^N_{|30 < \eta^+ < \eta_I^+}}, \quad (4.7)$$

conditional on the presence of an outer large-scale tangential velocity structure as a surrogate for the Görtler structures. The results are reported in figure 24. In both the REF and FRC flows, the peak perturbation stresses are recorded at  $\Delta\xi < 0$ , which is consistent with an inclination of the outer structures relative to the wall. However, in the forced case, the magnitude of perturbations in the wall stress is larger, and the footprint of the outer large scales is greater in extent. In fact, the affected region extends over a longer streamwise distance  $\Delta\xi$  (both positive and negative  $\Delta\xi$ ) due to the coherence of the outer large scales in this case (c.f. figures 16 and 17). In addition, the opposite wall stress perturbations are observed in the span which is consistent with the influence of

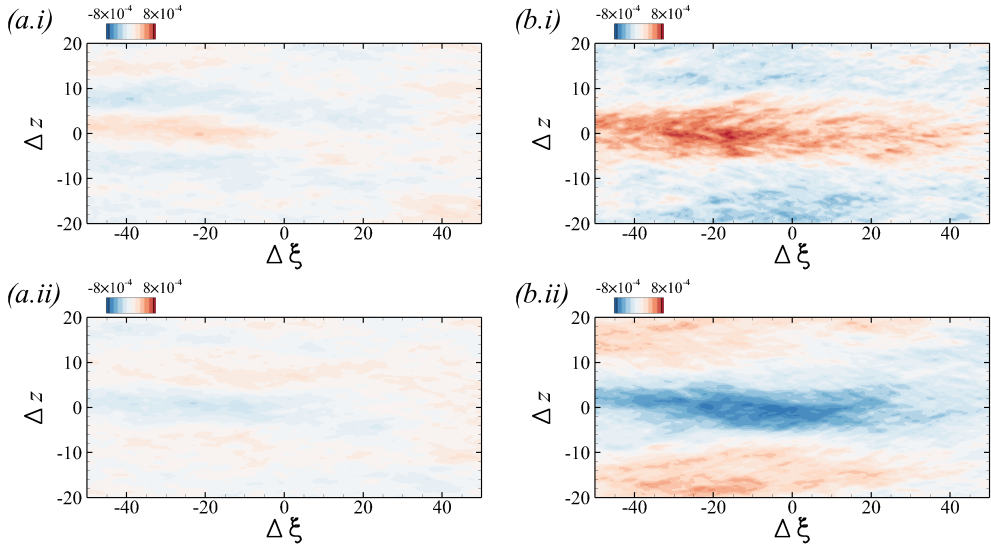


FIGURE 24. Conditionally averaged skin-friction coefficient from (a) REF and (b) FRC at  $\xi = 100$  ( $30^\circ$  station). (i)  $|c_f^P| \leq 8 \times 10^{-4}$  and (ii)  $|c_f^N| \leq 8 \times 10^{-4}$ .

roll motions displacement momentum away and towards the wall at spanwise locations that are separated by their width.

The results presented here provide a structural interpretation of the statistical changes of the boundary layer on the curved surface, without and with free-stream turbulence. While Görtler structures may be elusive in the former case, they are more prominent in the forced flow. Their higher amplitude, larger size and strong coherence are evident in the spectra and in conditional averages. The more energetic Görtler structures also promote the recovery of the boundary layer downstream of the APG at the onset of curvature, increase mixing in the wall-normal direction, and appreciably enhance the wall stress in their footprint.

## 5. Conclusion

Direct numerical simulations of turbulent boundary layers on a concave curve without and with free-stream turbulence were contrasted. In the latter case, the inlet turbulence was homogeneous and isotropic with intensity  $Tu = 10\%$ . The boundary layer and the free-stream turbulence were differentiated using a levelset approach which provides an objective, virtual interface.

Near the onset of the curvature, the drag significantly drops due to the adverse pressure gradient which induces intermittent flow separation. The forcing by free-stream turbulence reduces the probability of separation and promotes the downstream recovery of the flow along the ZPG section of the curve. The external forcing also increases the skin friction by up to 49% relative to the reference flow (figure 6).

The curved wall has a clear impact on the wall-normal and spanwise normal stresses, both indicative of the development of Görtler vortices in the outer region (figure 9). The wall-normal separation between the peaks of these components of stress increases with downstream distance, signaling the growth of the vortices as the boundary layer expands (figure 10). When the FST is present, the outer roll motions are more energetic and



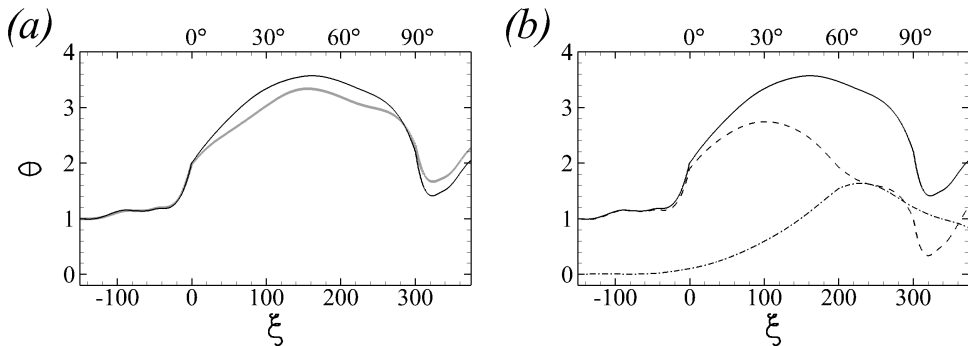


FIGURE 25. (a) Development of momentum thickness  $\theta$  in (gray) REF and (black) FRC. (b) For FRC, (—)  $\theta$  is further decomposed into the two contributions (--- and -.-) on the right hand side of equation (A 2).

larger is size. In addition, and in contrast to flat-plate boundary layers, introducing FST increases the peak shear-stress correlation coefficient in the curved wall flow (figure 13b).

Above the curved section, the turbulence structures are significantly modified. Curvature spurs the formation of outer roll motions which increase in size on the concave wall as seen in the conditionally averaged flow fields (figures 16 and 17). In the forced flow, these longitudinal structures, which we interpret as Görlter vortices, are enlarged in size, strengthened in intensity, display a clear streamwise coherence, and enhanced wall-normal mixing. As a result, the probability of observing free-stream fluid remains finite within the buffer layer (figure 20), in contrast to earlier results for flat-plate boundary layers where external turbulence could not reach the buffer layer (You & Zaki 2019). The impact on the near-wall region is direct (figure 21), in particular in the wall stress at their footprint (figure 24).

## Acknowledgements

This work is sponsored by the National Science Foundation (grant 1605404). Computational resources were provided by the Maryland Advanced Research Computing Center (MARCC).

## Appendix A. The momentum thickness

The momentum thickness is an important proxy of the state of the boundary layer. Various definitions have been proposed for curved-wall flows, and we here consider the form adopted by Patel (1969),

$$\theta = \int_0^{\eta_p} \frac{\overline{u_\xi}}{U_{pw,R}} \left( \frac{U_{p,R}}{U_{pw,R}} - \frac{\overline{u_\xi}}{U_{pw,R}} \right) d\eta. \quad (\text{A } 1)$$

The subscript  $R$  indicates that we are adopting the profile of the potential velocity from the REF case, which is not necessarily preserved in the FRC case. For this reason, we also perform the integration up to the wall-normal position  $\eta_p$  where the potential-velocity profiles from both REF and FRC intersect. The downstream dependence of  $\theta$  is reported in figure 25a which shows the anticipated increase in the momentum thickness near  $\xi = 0$  due to flow deceleration. On the curved wall  $\theta$  is larger in the FRC case; this effect is seemingly consistent with flat-plate boundary layers where the change in  $\theta$  can be directly related to increase in skin friction under free-stream turbulence forcing. The reality is,

however, more complex as can be shown by re-expressing the momentum thickness as,

$$\theta = \frac{(U_{pw})^2}{(U_{pw,R})^2} \int_0^{\eta_p} \underbrace{\frac{\bar{u}_\xi}{U_{pw}} \left( \frac{U_p}{U_{pw}} - \frac{\bar{u}_\xi}{U_{pw}} \right)}_{=\tilde{\theta}} d\eta + \int_0^{\eta_p} \frac{\bar{u}_\xi}{U_{pw,R}} \left( \frac{U_{p,R}}{U_{pw,R}} - \frac{U_p}{U_{pw,R}} \right) d\eta. \quad (\text{A } 2)$$

The first term involves a momentum thickness  $\tilde{\theta}$  defined using the potential velocity of each flow (instead of adopting  $U_{p,R}$  for both REF and FRC), and the second term is due to the difference of the potential velocities in the two simulations. Figure 25b shows that the increase in  $\theta$  in FRC is due to this second term. The thicker boundary layer in the forced case increases the effective curvature, specifically  $\bar{\eta}_l/R$  or similarly  $\delta_{99}/R$ , and hence turning of the outer flow. The result is a steeper  $U_p$  profile in the free stream, a lower  $U_p$  inside the boundary layer and increased deficit  $U_{p,R} - U_p$ . Interpreting the momentum thickness must therefore take this effect into account.

## REFERENCES

- AMES, F. E. & MOFFAT, R. J. 1990 Heat transfer with high intensity, large scale turbulence: the flat plate turbulent boundary layer and the cylindrical stagnation point. *Stanford University Report* pp. HMT-44.
- AROLLA, S. K. & DURBIN, P. A. 2015 LES of spatially developing turbulent boundary layer over a concave surface. *J. Turbul.* **16** (1), 81–99.
- BANDYOPADHYAY, P. R. & AHMED, A. 1993 Turbulent boundary layers subjected to multiple curvatures and pressure gradients. *J. Fluid Mech.* **246**, 503–527.
- BARLOW, R. S. & JOHNSTON, J. P. 1988a Structure of a turbulent boundary layer on a concave surface. *J. Fluid Mech.* **191**, 137–176.
- BARLOW, R. S. & JOHNSTON, J. P. 1988b Local effects of large-scale eddies on bursting in a concave boundary layer. *J. Fluid Mech.* **191**, 177–195.
- BERNARDINI, M. & PIROZZOLI, S. 2011 Inner/outer layer interactions in turbulent boundary layers: A refined measure for the large-scale amplitude modulation mechanism. *Phys. Fluids* **23**, 061701.
- CASTRO, I. P. 1984 Effects of free-stream turbulence on low Reynolds number boundary layers. *Trans. ASME: J. Fluids Engng* **106**, 298–306.
- DOGAN, E., HANSON, R. E. & GANAPATHISUBRAMANI, B. 2016 Interactions of large-scale free-stream turbulence with turbulent boundary layers. *J. Fluid Mech.* **802**, 79–107.
- FLORYAN, J. M. 1991 On the Görtler instability of boundary layers. *Progress in Aerospace Sciences* **28** (3), 235–271.
- GUNGOR, A. G., MACIEL, Y., SIMENS, M. P. & SORIA, J. 2016 Scaling and statistics of large-defect adverse pressure gradient turbulent boundary layers. *Int. J. Heat Fluid Flow* **59**, 109–124.
- HALL, P 1982 Taylor-Gortler vortices in fully developed or boundary-layer flows: linear theory. *Journal of Fluid Mechanics* **124**, 475–494.
- HANCOCK, P. E. & BRADSHAW, P. 1983 The effect of free-stream turbulence on turbulent boundary layers. *Trans. ASME: J. Fluids Engng.* **105**, 284–289.
- HANCOCK, P. E. & BRADSHAW, P. 1989 Turbulence structure of a boundary layer beneath a turbulent free stream. *J. Fluid Mech.* **205**, 45–76.
- HARUN, Z., MONTY, J. P., MATHIS, R. & MARUSIC, I. 2013 Pressure gradient effects on the large-scale structure of turbulent boundary layers. *J. Fluid Mech.* **715**, 477–498.
- HEARST, R. J., DOGAN, E. & GANAPATHISUBRAMANI, B. 2018 Robust features of a turbulent boundary layer subjected to high-intensity free-stream turbulence. *J. Fluid Mech.* **851**, 416–435.
- HICKEL, S. & ADAMS, N. A. 2008 Implicit LES applied to zero-pressure-gradient and adverse-pressure-gradient boundary layer turbulence. *Int. J. Heat Fluid Flow* **29**, 626–639.
- HOFFMANN, P. H., MUCK, K. C. & BRADSHAW, P. 1985 The effect of concave surface curvature on turbulent boundary layers. *J. Fluid Mech.* **161**, 371–403.

- HUNT, J. C. R. & DURBIN, P. A. 1999 Perturbed vortical layers and shear sheltering. *Fluid Dyn. Res.* **24** (6), 375–404.
- HUTCHINS, N. & MARUSIC, I. 2007 Evidence of very long meandering features in the logarithmic region of turbulent boundary layers. *J. Fluid Mech.* **579**, 1–28.
- HWANG, J., LEE, J., SUNG, H. J. & ZAKI, T. A. 2016 Inner-outer interactions of large-scale structures in turbulent channel flow. *J. Fluid Mech.* **790**, 128–157.
- JELLY, T. O., JUNG, S. Y. & ZAKI, T. A. 2014 Turbulence and skin friction modification in channel flow with streamwise-aligned superhydrophobic surface texture. *Phys. Fluids* **26**, 095102.
- JUNG, S. Y. & ZAKI, T. A. 2015 The effect of a low-viscosity near-wall film on bypass transition in boundary layers. *J. Fluid Mech.* **772**, 330–360.
- KESTORAS, M. D. & SIMON, T. W. 1995 Effects of free-stream turbulence intensity on a boundary layer recovering from concave curvature effects. *Trans. ASME: Turbomachinery* **117**, 240–247.
- KESTORAS, M. D. & SIMON, T. W. 1998 Conditionally sampled measurements in a heated turbulent boundary layer: Curvature and free-stream turbulence effects. *Exp. Therm. Fluid Sci.* **17**, 63–70.
- KOZUL, M., HEARST, R. J., MONTY, J. P., GANAPATHISUBRAMANI, B. & CHUNG, D. 2020 Response of the temporal turbulent boundary layer to decaying free-stream turbulence. *J. Fluid Mech.* **896**, A11.
- LEE, J., LEE, J. H., CHOI, J.-I. & SUNG, H. J. 2014 Spatial organization of large-and very-large-scale motions in a turbulent channel flow. *Journal of fluid mechanics* **749**, 818–840.
- LEE, J., SUNG, H. J. & ZAKI, T. A. 2017 Signature of large-scale motions on turbulent/non-turbulent interface in boundary layers. *J. Fluid Mech.* **819**, 165–187.
- LIGHTHILL, M. J. 1963 *Boundary Layer Theory*. Oxford University Pres.
- LOPES, A. S., PIOMELLI, U. & PALMA, J. M. L. M. 2006 Large-eddy simulation of the flow in an s-duct. *J. Turbul.* **7** (11), 1–24.
- LUND, T. S. & MOIN, P. 1996 Large-eddy simulation of a concave wall boundary layer. *Int. J. Heat Fluid Flow* **17**, 290–295.
- MATHIS, R., HUTCHINS, N. & MARUSIC, I. 2009 Large-scale amplitude modulation of the small-scale structures in turbulent boundary layers. *J. Fluid Mech.* **628**, 311–337.
- MOSER, R. D. & MOIN, P. 1987 The effects of curvature in wall-bounded turbulent flows. *Journal of Fluid Mechanics* **175**, 479–510.
- MOTOORI, YUTARO & GOTO, SUSUMU 2019 Generation mechanism of a hierarchy of vortices in a turbulent boundary layer. *Journal of Fluid Mechanics* **865**, 1085–1109.
- PATEL, V. C. 1969 The effects of curvature on the turbulent boundary layer. *Aeronautical Research Council, London* pp. R&M 3599,.
- PATEL, V. C. & SOTIROPOULOS, F. 1997 Longitudinal curvature effects in turbulent boundary layers. *Prog. Aerosp. Sci.* **33**, 1–70.
- ROSENFELD, M., KWAK, D. & VINOKUR, M. 1991 A fractional step solution method for the unsteady incompressible navier-stokes equations in generalized coordinate systems. *J. Comput. Phys.* **94**, 102–137.
- SARIC, W. S. 1994 Görtler vortices. *Annual Review of Fluid Mechanics* **26** (1), 379–409.
- SCHRADER, L. U., BRANDT, L. & ZAKI, T. A. 2011 Receptivity, instability and breakdown of Görtler flow. *J. Fluid Mech.* **682**, 362–396.
- SIMONICH, J. C. & BRADSHAW, P. 1978 Effect of free-stream turbulence on heat transfer through a turbulent boundary layer. *Trans. ASME: J. Heat Transfer* **100**, 671–677.
- SMITH, A. M. O. 1955 On the growth of Taylor-Görtler vortices along highly concave walls. *Quarterly of Applied Mathematics* **13** (3), 233–262.
- TANI, I. 1962 Production of longitudinal vortices in the boundary layer along a concave wall. *J. Geophys. Res.* **67**, 3075–3080.
- THOLE, K. A. & BOGARD, D. G. 1995 Enhanced heat transfer and shear stress due to high free-stream turbulence. *Trans. ASME: J. Turbomachinery* **117**, 418–424.
- THOLE, K. A. & BOGARD, D. G. 1996 High freestream turbulence effects on turbulent boundary layers. *Trans. ASME: J. Fluids Engng* **118**, 276–284.
- THOMPSON, J. F., WARSI, Z. U. A. & MASTIN, C. W. 1985 *Numerical Grid Generation: Foundations and Applications*. North Holland.

- WANG, MENGZE, WANG, QI & ZAKI, TAMER A. 2019 Discrete adjoint of fractional-step incompressible Navier-Stokes solver in curvilinear coordinates and application to data assimilation. *Journal of Computational Physics* **396**, 427–450.
- YOU, J. & ZAKI, T. A. 2019 Conditional statistics and flow structures in turbulent boundary layers buffeted by free-stream disturbances. *J. Fluid Mech.* **866**, 526–566.
- YOU, J. & ZAKI, T. A. 2020 Turbulent heat-transfer enhancement in boundary layers exposed to free-stream turbulence. *Flow, Turbulence and Combustion* **104(2)**, 381–402.
- ZAKI, TAMER A. & DURBIN, PAUL A. 2006 Continuous mode transition and the effects of pressure gradient. *Journal of Fluid Mechanics* **563**, 357–388.
- ZAKI, T. A. & SAHA, S. 2009 On shear sheltering and the structure of vortical modes in single- and two-fluid boundary layers. *J. Fluid Mech.* **626**, 111–147.
- ZAKI, TAMER A., WISSINK, J. G., RODI, WOLFGANG & DURBIN, P. A. 2010 Direct numerical simulations of transition in a compressor cascade: the influence of free-stream turbulence. *Journal of Fluid Mechanics* **665**, 57–98.